

## MULTIWAVELENGTH MASS COMPARISONS OF THE $z \sim 0.3$ CNOC CLUSTER SAMPLE

A. K. HICKS

Department of Astronomy, University of Virginia, P.O. Box 400325, Charlottesville, VA 22904; ahicks@alum.mit.edu

E. ELLINGSON

Center for Astrophysics and Space Astronomy, University of Colorado, Campus Box 389,  
Boulder, CO 80309; elling@casa.colorado.edu

H. HOEKSTRA

Department of Physics and Astronomy, University of Victoria, Elliott Building, 3800 Finnerty Road,  
Victoria, BC V8P 5C2, Canada; hoekstra@uvic.ca

AND

H. K. C. YEE

Department of Astronomy and Astrophysics, University of Toronto, 60 St. George Street,  
Toronto, ON M5S 3H8, Canada; hyee@astro.utoronto.ca

Received 2006 March 29; accepted 2006 August 1

### ABSTRACT

Results are presented from a detailed analysis of optical and X-ray observations of moderate-redshift galaxy clusters from the Canadian Network for Observational Cosmology (CNOC) subsample of the EMSS. The combination of extensive optical and deep X-ray observations of these clusters make them ideal candidates for multi-wavelength mass comparison studies. X-ray surface brightness profiles of 14 clusters with  $0.17 < z < 0.55$  are constructed from *Chandra* observations and fit to single- and double- $\beta$  models. Spatially resolved temperature analysis is performed, indicating that five of the clusters in this sample exhibit temperature gradients within their inner 60–200 kpc. Integrated spectra extracted within  $R_{2500}$  provide temperature, abundance, and luminosity information. Under assumptions of hydrostatic equilibrium and spherical symmetry, we derive gas and total masses within  $R_{2500}$  and  $R_{200}$ . We find an average gas mass fraction of  $f_{\text{gas}}(R_{200}) = 0.092 \pm 0.004 h_7^{-3/2}$ , resulting in  $\Omega_m = 0.42 \pm 0.02$  (formal error). We also derive dynamical masses for these clusters to  $R_{200}$ . We find no systematic bias between X-ray and dynamical methods across the sample, with an average  $M_{\text{dyn}}/M_X = 0.97 \pm 0.05$ . We also compare X-ray masses to weak-lensing mass estimates of a subset of our sample, resulting in a weighted average of  $M_{\text{lens}}/M_X$  of  $0.99 \pm 0.07$ . We investigate X-ray-scaling relationships and find power-law slopes that are slightly steeper than the predictions of self-similar models, with an  $E(z)^{-1}L_X-T_X$  slope of  $2.4 \pm 0.2$  and an  $E(z)M_{2500}-T_X$  slope of  $1.7 \pm 0.1$ . Relationships between red-sequence optical richness ( $B_{\text{gc,red}}$ ) and global cluster X-ray properties ( $T_X$ ,  $L_X$ , and  $M_{2500}$ ) are also examined and fitted.

*Subject headings:* cosmology: observations — galaxies: clusters: general — X-rays: galaxies: clusters

### 1. INTRODUCTION

Clusters of galaxies are valuable cosmological probes. As the largest gravitationally bound objects in the universe, they play a key role in the tracing and modeling of large-scale structure formation and evolution (e.g., Voit 2005; Bahcall et al. 1997). Because of our rapidly expanding sample of known clusters, finding efficient means of estimating cluster properties is a highly desirable goal.

The contribution of cluster studies to the field of observational cosmology hinges on our ability to accurately estimate cluster masses. In particular, through the determination of both gas mass and total mass, cluster analysis can lead to estimations of the cosmological mass density,  $\Omega_m$ , while accurate measurement of the evolution of the cluster mass function provides important constraints on both the normalization of the matter power spectrum,  $\sigma_8$ , and the dark energy equation of state,  $w$  (e.g., Levine et al. 2002; Eke et al. 1998). In addition, gaining an understanding of the evolution of X-ray-scaling relationships (such as  $L_X-T_X$  and  $M-T_X$ ) with redshift provides an important contribution to our ability to accurately model the evolution of large-scale structure in the universe (e.g., Voit 2005).

Intermediate-redshift ( $0.2 < z < 0.6$ ) clusters are well situated for the study of cluster properties. They are compact enough to be observed without tedious mosaicking, and they are present in statistically significant numbers. Intermediate-redshift clusters are also luminous enough to permit detailed investigation, with the potential for placing strong constraints on cluster evolution.

Three frequently applied approaches to estimating cluster masses are gravitational lens modeling, optical spectroscopic measurements of the cluster galaxy velocity dispersion, and characterizing X-ray emission as a means of tracing the underlying potential well of the cluster. Each of these methods uses different observations and assumptions, which can be tested through their direct comparison. An alternate optical approach to the efficient estimation of cluster masses involves the use of optical richness. This method relies on the assumption that galaxy light is a reliable tracer of total cluster mass and requires calibration via other methods.

Lensing mass estimates test both the assumption of hydrostatic equilibrium and our knowledge of the mass distribution in clusters. Because they probe all of the projected mass along the line of sight, which may include additional mass concentrations, they are susceptible to overestimation of cluster mass (Cen 1997; Metzler et al. 2001). Dynamical mass estimates work under the

TABLE 1  
 CLUSTER SAMPLE

CLUSTER	$z$	CENTROID		$l''$ ( $h_{70}^{-1}$ kpc)	OBSID	ARRAY	<i>Chandra</i> EXPOSURE <sup>a</sup> (s)
		R.A.	Decl.				
Abell 2390 .....	0.2279	21 53 36.794	+17 41 41.85	3.65	4193	ACIS-S	89624
MS 0015.9+1609 .....	0.5466	00 18 33.64	+16 26 11.2	6.39	520	ACIS-I	69235
MS 0302.7+1658 .....	0.4246	03 05 31.72	+17 10 01.5	5.57	525	ACIS-I	11764
MS 0440.5+0204 .....	0.1965	04 43 09.974	+02 10 18.01	3.17	4196	ACIS-S	45104
MS 0451.5+0250 .....	0.2010	...	...	3.31	4215	ACIS-I	66275
MS 0451.6–0305 .....	0.5392	04 54 11.19	–03 00 52.2	6.34	902	ACIS-S	43652
MS 0839.8+2938 .....	0.1928	08 42 55.999	+29 27 25.45	3.21	2224	ACIS-S	31383
MS 0906.5+1110 .....	0.1709	09 09 12.81	+10 58 31.7	2.91	924	ACIS-I	31392
MS 1006.0+1202 .....	0.2605	10 08 47.56	+11 47 34.0	4.03	925	ACIS-I	25590
MS 1008.1–1224 .....	0.3062	10 10 32.44	–12 39 41.4	4.52	926	ACIS-I	37376
MS 1358.4+6245 .....	0.3290	13 59 50.640	+62 31 04.20	4.74	516	ACIS-S	53055
MS 1455.0+2232 .....	0.2570	14 57 15.110	+22 20 32.26	3.99	4192	ACIS-I	91886
MS 1512.4+3647 .....	0.3726	15 14 22.507	+36 36 20.15	5.14	800	ACIS-S	14665
MS 1621.5+2640 .....	0.4274	16 23 35.37	+26 34 19.4	5.59	546	ACIS-I	30062

NOTE.—Units of right ascension are hours, minutes, and seconds, and units of declination are degrees, arcminutes, and arcseconds.

<sup>a</sup> Corrected exposure time (see text for corrections applied).

assumption that velocity dispersion is directly related to the underlying gravitational potential of the cluster. Pitfalls of this technique also include the danger of overestimating the cluster mass in cases in which substructure or mergers drive up velocity dispersion measurements (Bird et al. 1995).

The hot, diffuse intracluster medium (ICM), which is observed in the X-ray, should be a direct tracer of a cluster’s underlying potential well. Under assumptions of isothermality and hydrostatic equilibrium, the surface brightness of a cluster of galaxies can provide information on gas density as well as total gravitating mass. Factors that influence the accuracy of X-ray mass estimates are temperature gradients, substructure, and mergers, which can compromise the previously stated assumptions (e.g., Balland & Blanchard 1997).

One of the main objectives of this work is to identify, through direct comparison, any systematic biases in these methods with the ultimate goal of determining a robust calibration between optical richness and cluster mass. Optical richness measurements are easily available due to the fact that their estimation requires very little observing time. Therefore, an accurate calibration of the relationship between mass and optical richness would allow us to determine the masses of large samples of clusters in a highly efficient manner, providing strong constraints on the evolution of the cluster mass function and, consequently, key cosmological parameters.

In this paper we present a detailed analysis of high-resolution *Chandra* X-ray observations of 14 CNOC (Yee et al. 1996b) clusters at  $z \sim 0.3$ . In §§ 2–4 we probe the temperature, metallicity, morphology, and surface brightness of the hot ICM present in each cluster. From this initial analysis we derive mass estimates (§ 5), which are compared to dynamical and weak-lensing mass estimates (§ 7), and then we examine the X-ray scaling laws of our sample (§ 8). Finally, in § 9 we use our results to calibrate relationships between red-sequence optical richness ( $B_{gc, red}$ ) and global cluster X-ray properties ( $T_X$ ,  $L_X$  and  $M_{2500}$ ). Unless otherwise noted, this paper assumes a cosmology of  $H_0 = 70 \text{ km s}^{-1} \text{ Mpc}^{-1}$ ,  $\Omega_m = 0.3$ , and  $\Omega_\Lambda = 0.7$ .

## 2. CLUSTER SAMPLE AND *CHANDRA* OBSERVATIONS

X-ray observations of our sample were retrieved from the *Chandra* Data Archive (CDA) after conducting a search for cur-

rently available *Chandra* observations of the CNOC (Yee et al. 1996b) intermediate-redshift ( $0.17 < z < 0.55$ ) subsample of 15 Extended Medium-Sensitivity Survey (EMSS) clusters (Gioia et al. 1990; Henry et al. 1992) and one Abell cluster (Abell 1958). The selection criterion for this sample can be found in Yee et al. (1996b). This sample has been extensively observed by the CNOC cluster survey (CNOC-1), and galaxy redshifts of  $\sim 1200$  cluster members as well as detailed photometric catalogs are available for these clusters (e.g., Yee et al. 1996a).

*Chandra* Advanced CCD Imaging Spectrometer (ACIS) observations of 14 of the 16 CNOC clusters were obtained. Six of these clusters were observed with the ACIS-S CCD array, and eight were observed with ACIS-I, with an overall range in individual exposures of 11.7–91.9 ks. Three of the clusters in our sample were observed on multiple occasions, in which case we have chosen the longest of those observations to include in our analysis. Each of the observations analyzed in this study possesses a start date that falls on or after 2000 April 24 indicating a focal plane temperature of  $-120^\circ\text{C}$  for the entire sample.

Aspect solutions were examined for irregularities and none were found. Background contamination due to charged particle flares were reduced by removing time intervals during which the background rate exceeded the average background rate by more than 20%. The event files were filtered on standard grades and bad pixels were removed. A two-dimensional elliptical Lorentzian was fit to the counts image of each data set to locate the center of the X-ray emission peak. All centroid position errors are within a resolution element ( $\sim 0''.5$ ). In the case of the heavily substructured cluster MS 0451+02, a fitted central peak was unobtainable, so a position at the center of the extended emission was chosen for spectral analysis at an R.A. and decl. of  $04^{\text{h}}54^{\text{m}}09^{\text{s}}941$ ,  $+02^\circ 55' 14''.52$  (J2000.0), and the surface brightness profile was centered on the slightly offset peak of emission at an R.A. and decl. of  $04^{\text{h}}54^{\text{m}}07^{\text{s}}249$ ,  $+02^\circ 54' 27''.31$  (J2000.0). Table 1 provides a list of each of the clusters in our sample, including redshifts, ObsID, detector array, and corrected exposure information for each observation.

After initial cleaning of the data, 0.6–7.0 keV images, instrument maps, and exposure maps were created using the CIAO 3.2 tools `dmcopy`, `mkinstmap`, and `mkexmap`. Data with energies

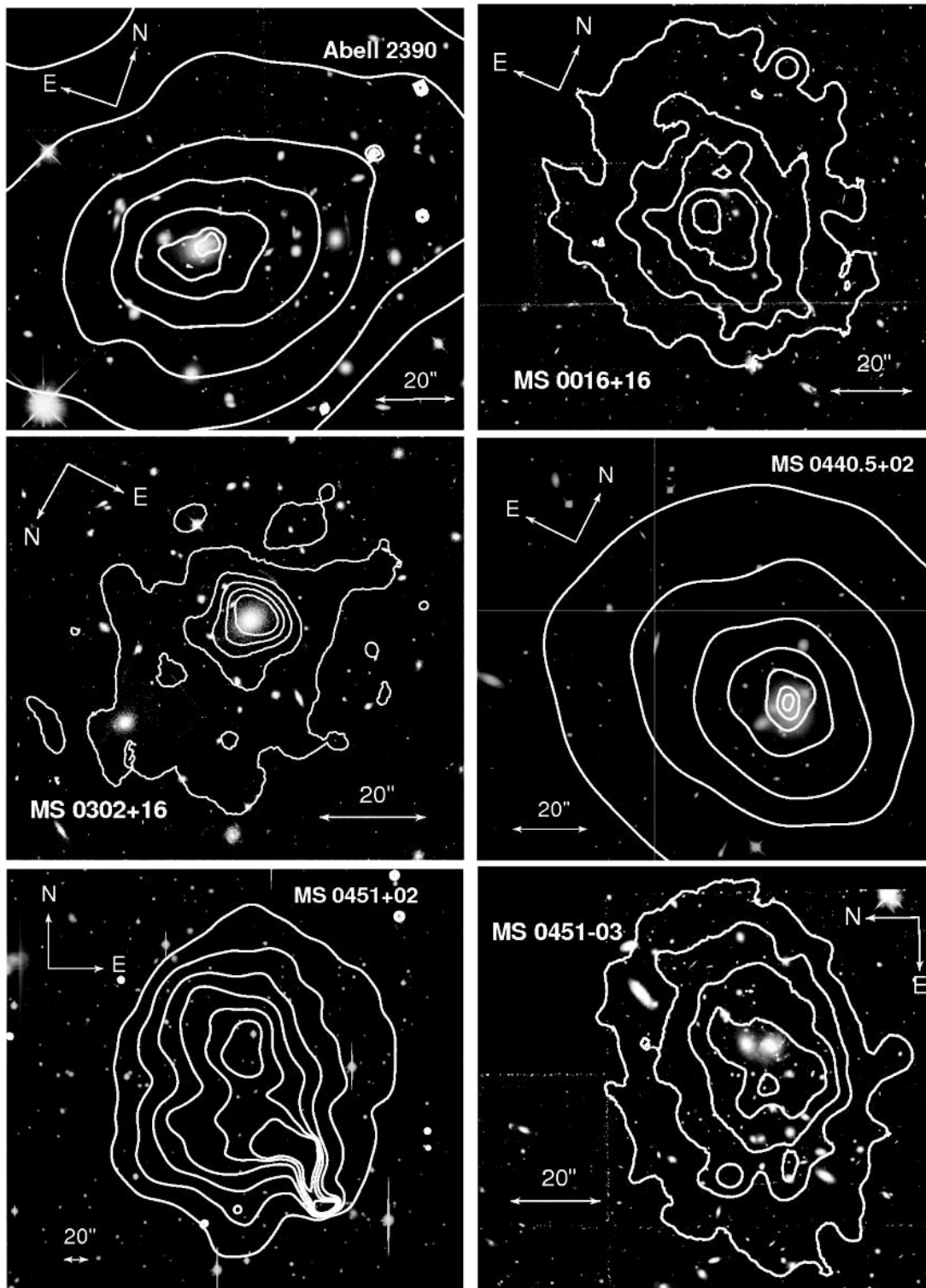


FIG. 1.—Optical images. X-ray contours are overlaid on optical images of clusters in our sample. *HST* images of Abell 2390, MS 0016+16, MS 0302+16, MS 0440.5+02, MS 0451-03, MS 1358+62, MS 1455+22, MS 1512+36, and MS 1621+26 were retrieved from the MAST archive, with respective filters F814W, F555W, F814W, F702W, F702W, F814W, F606W, F555W, and F814W. Gunn  $r$ -band (to  $r \sim 24$ ) CFHT images for the remaining five clusters (MS 0451+02, MS 0839+29, MS 0906+11, MS 1006+12, and MS 1008-12) are from the CNOC1 survey (Yee et al. 1996a). X-ray contours were created from adaptively smoothed *Chandra* 0.6–7.0 keV flux images, and all have linear values except for three of the cooling core clusters (Abell 2390, MS 0440+02, and MS 1455+22), which are overlaid with logarithmic X-ray contours. Note the significant amount of substructure present in MS 0451+02.

below 0.6 keV and above 7.0 keV were excluded due to uncertainties in the ACIS calibration and background contamination, respectively.

Flux images were created by dividing the resulting images by their respective exposure maps. Point source detection was per-

formed by running the tools `wtransform` and `wrecon` on the flux images. Adaptively smoothed flux images were created with `csmooth`. Figure 1 contains Canada-France-Hawaii Telescope (CFHT) images obtained from the CNOC database (Yee et al. 1996b), and, where available, *Hubble Space Telescope* (*HST*)

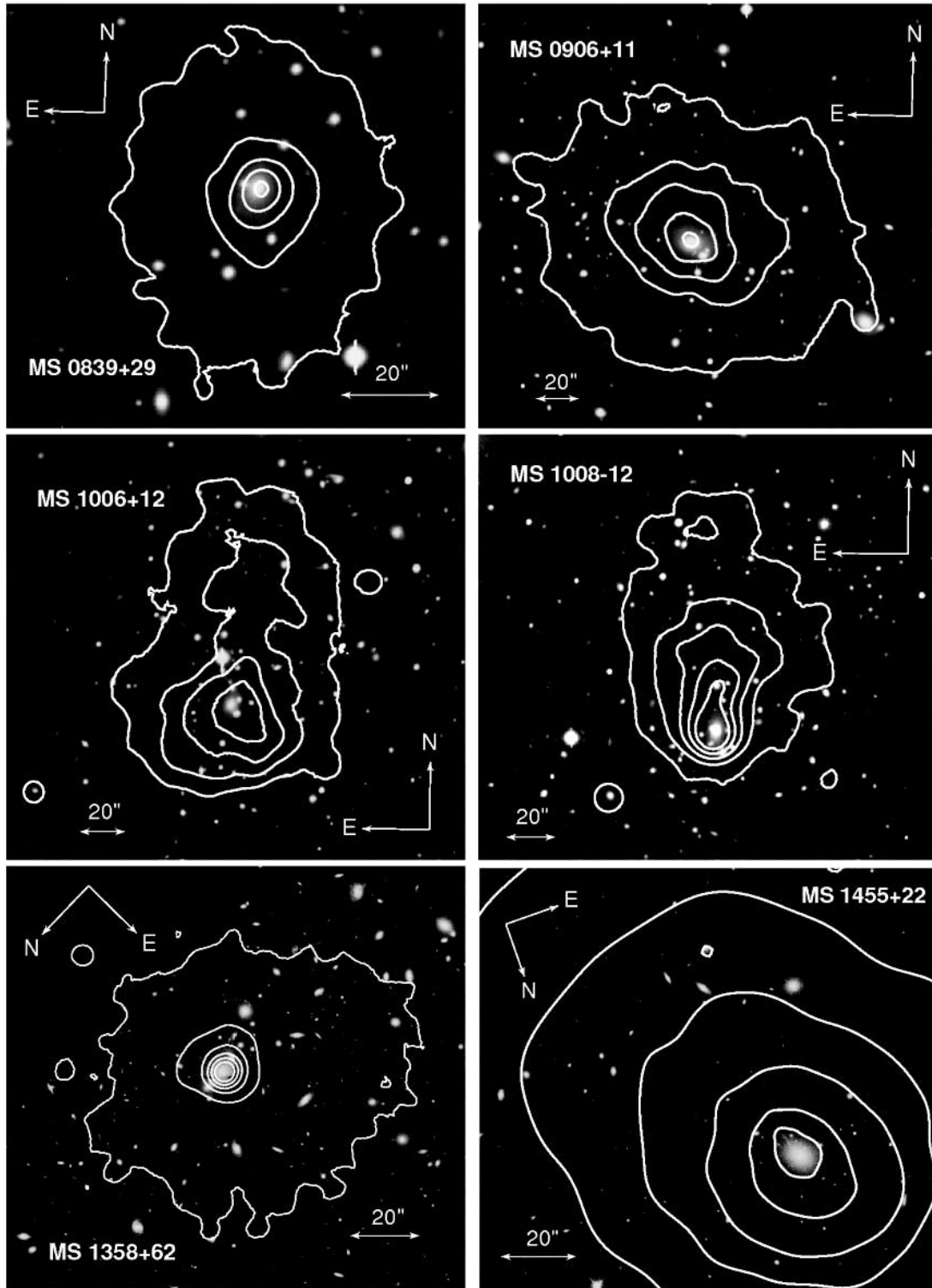


FIG. 1.—Continued

images obtained from the Multimission Archive at the Space Telescope Science Institute (MAST) archive, each of which is overlaid with X-ray contours created from smoothed *Chandra* flux images.

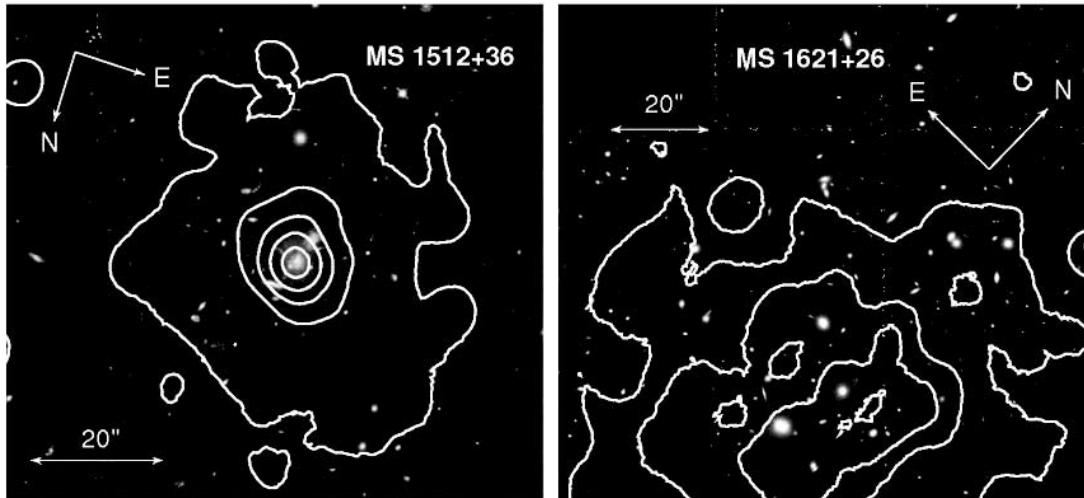
### 3. SURFACE BRIGHTNESS

Using the 0.6–7.0 keV images and exposure maps, a radial surface brightness profile was computed in 1'' annular bins for each

cluster. These profiles were then fit with both single- and double- $\beta$  models. Single- $\beta$  models take the form

$$I(r) = I_B + I_0 \left( 1 + \frac{r^2}{r_c^2} \right)^{-3\beta+1/2}, \quad (1)$$

where  $I_B$  is a constant representing the surface brightness contribution of the background,  $I_0$  is the normalization, and  $r_c$  is the core radius.

FIG. 1.— *Continued*

The double- $\beta$  model has the form

$$I(r) = I_B + I_1 \left(1 + \frac{r^2}{r_1^2}\right)^{-3\beta_1+1/2} + I_2 \left(1 + \frac{r^2}{r_2^2}\right)^{-3\beta_2+1/2}, \quad (2)$$

where each component has fit parameters  $(I_n, r_n, \beta_n)$ .

Although a fair number of the clusters in our sample possess detectably elliptical or irregular emission, circular surface brightness profiles were chosen based on a number of factors. First, as discussed in Neumann & Bohringer (1997) and Böhringer et al. (1998), differences in masses derived using elliptical versus circular  $\beta$ -profiles are small ( $\sim 5\%$ ). Second, circular  $\beta$ -profiles provide a more straightforward comparison between dynamical and X-ray-derived masses, since dynamical mass calculations assume sphericity. Finally, temperature uncertainties should outweigh any errors introduced by assuming radial symmetry.

The parameters of the best-fitting single- $\beta$  model of each cluster are shown in Table 2. While nine of the clusters' surface brightness profiles do not exhibit excess unmodeled emission in their cores when fit with a single- $\beta$  model, five of the clusters do exhibit excess emission in their cores. The surface brightness pro-

files of these clusters are better fit with the addition of a second  $\beta$ -component. All of the clusters requiring a double- $\beta$  model, Abell 2390, MS 0440+02, MS 0839+29, MS 1358+62, and MS 1455+22 (Lewis et al. 1999; Allen 2000), are believed to contain cooling flows and exhibit strong ( $L_{\text{H}\alpha + [\text{N III}]} > 10^{42}$  ergs  $\text{s}^{-1}$ ) extended H $\alpha$  emission (Donahue et al. 1992; Lewis et al. 1999). Best-fitting double- $\beta$  model parameters are given in Table 3. Surface brightness profiles of the clusters in our sample are shown in Figure 2. Discrepancies in background values are due to the use of both ACIS-I and ACIS-S arrays (ACIS-S typically has background values that are a factor of 3 higher than ACIS-I).

#### 4. SPECTRAL ANALYSIS OF X-RAY OBSERVATIONS

##### 4.1. Integrated Spectra and $R_{2500}$

For the purpose of fitting cluster-scaling relationships within a well-defined region of mass overdensity, global cluster properties were determined for our sample within  $R_{2500}$ . Using the fitted X-ray centroid positions obtained in § 2 (with the exception of MS 0451+02, as noted in § 2), a spectrum was extracted from each cleaned event file in a circular region with a  $300 h_{70}^{-1}$  kpc

TABLE 2  
 $\beta$ -MODEL FITS

Cluster	$R_c$ ( $h_{70}^{-1}$ kpc)	$\beta$	$I_0$ ( $10^{-9}$ photons $\text{s}^{-1}$ $\text{cm}^{-2}$ arcsec $^{-2}$ )	$I_B$ ( $10^{-9}$ photons $\text{s}^{-1}$ $\text{cm}^{-2}$ arcsec $^{-2}$ )	$\chi^2/\text{DOF}$
Abell 2390 .....	$63 \pm 2$	$0.531 \pm 0.003$	$1575^{+34}_{-35}$	$1.7 \pm 0.2$	368.8/145
MS 0015.9+1609 .....	$253 \pm 13$	$0.72 \pm 0.02$	$100 \pm 4$	$1.17 \pm 0.04$	316.2/230
MS 0302.7+1658 .....	$27^{+5}_{-4}$	$0.50 \pm 0.02$	$337^{+67}_{-56}$	$0.89 \pm 0.04$	328.2/324
MS 0440.5+0204 .....	$13^{+2}_{-1}$	$0.444 \pm 0.006$	$933^{+84}_{-93}$	$2.4 \pm 0.1$	372.2/191
MS 0451.5+0250 .....	$520^{+50}_{-43}$	$0.87^{+0.1}_{-0.08}$	$51 \pm 1$	$1.7 \pm 0.3$	620.4/227
MS 0451.6-0305 .....	$200 \pm 10$	$0.73 \pm 0.02$	$154 \pm 6$	$1.81 \pm 0.05$	257.3/205
MS 0839.8+2938 .....	$58 \pm 3$	$0.62^{+0.02}_{-0.01}$	$407^{+37}_{-27}$	$2.33 \pm 0.07$	220.7/208
MS 0906.5+1110 .....	$96^{+7}_{-6}$	$0.60 \pm 0.02$	$185^{+8}_{-7}$	$1.2 \pm 0.2$	177/174
MS 1006.0+1202 .....	$129^{+15}_{-13}$	$0.55^{+0.03}_{-0.02}$	$88^{+7}_{-6}$	$0.8^{+0.2}_{-0.1}$	270.7/213
MS 1008.1-1224 .....	$113 \pm 9$	$0.55 \pm 0.02$	$101^{+7}_{-6}$	$1.09 \pm 0.06$	329.4/218
MS 1358.4+6245 .....	$76 \pm 5$	$0.54 \pm 0.01$	$455^{+32}_{-30}$	$3.8 \pm 0.1$	349.6/207
MS 1455.0+2232 .....	$36.7 \pm 0.8$	$0.612 \pm 0.004$	$3277^{+78}_{-73}$	$2.29 \pm 0.06$	789.1/209
MS 1512.4+3647 .....	$22 \pm 3$	$0.51 \pm 0.01$	$86^{+14}_{-11}$	$0.19 \pm 0.01$	192.5/191
MS 1621.5+2640 .....	$184^{+28}_{-25}$	$0.56^{+0.05}_{-0.04}$	$34 \pm 3$	$1.38^{+0.09}_{-0.1}$	234/225

TABLE 3  
DOUBLE- $\beta$  MODEL FITS

Cluster	$R_{c1}$ ( $h_{70}^{-1}$ kpc)	$\beta_1$	$I_{01}$ ( $10^{-9}$ photons $s^{-1}$ $cm^{-2}$ arcsec $^{-2}$ )	$R_{c2}$ ( $h_{70}^{-1}$ kpc)	$\beta_2$	$I_{02}$ ( $10^{-9}$ photons $s^{-1}$ $cm^{-2}$ arcsec $^{-2}$ )	$I_B$ ( $10^{-9}$ photons $s^{-1}$ $cm^{-2}$ arcsec $^{-2}$ )	$\chi^2/DOF$
Abell 2390 .....	$20^{+4}_{-3}$	$0.53^{+0.1}_{-0.07}$	$1709^{+157}_{-176}$	$80^{+11}_{-7}$	$0.52^{+0.02}_{-0.01}$	$504.9^{+101}_{-84}$	$1.7 \pm 0.2$	177.6/106
Abell 0440.5+0204 .....	$11.7^{+1}_{-0.6}$	$1.0 \pm 0.2$	$1246^{+149}_{-134}$	$33^{+2}_{-4}$	$0.489^{+0.011}_{-0.007}$	$338^{+30}_{-17}$	$2.80^{+0.1}_{-0.09}$	221.5/191
MS 0839.8+2938 .....	$21 \pm 4$	$0.9^{+0.2}_{-0.1}$	$761^{+146}_{-105}$	$59^{+8}_{-7}$	$0.62 \pm 0.02$	$366^{+56}_{-61}$	$2.3 \pm 0.1$	190/167
MS 1358.4+6245 .....	$10^{+2}_{-1}$	$0.46^{+0.05}_{-0.02}$	$3042^{+423}_{-380}$	$121^{+24}_{-20}$	$0.63^{+0.1}_{-0.05}$	$188^{+38}_{-31}$	$4.0^{+0.3}_{-0.4}$	156/139
MS 1455.0+2232 .....	$36^{+8}_{-4}$	$1.1 \pm 0.2$	$2635^{+325}_{-383}$	$56^{+21}_{-18}$	$0.64 \pm 0.01$	$1306^{+261}_{-218}$	$2.45 \pm 0.07$	276.3/183

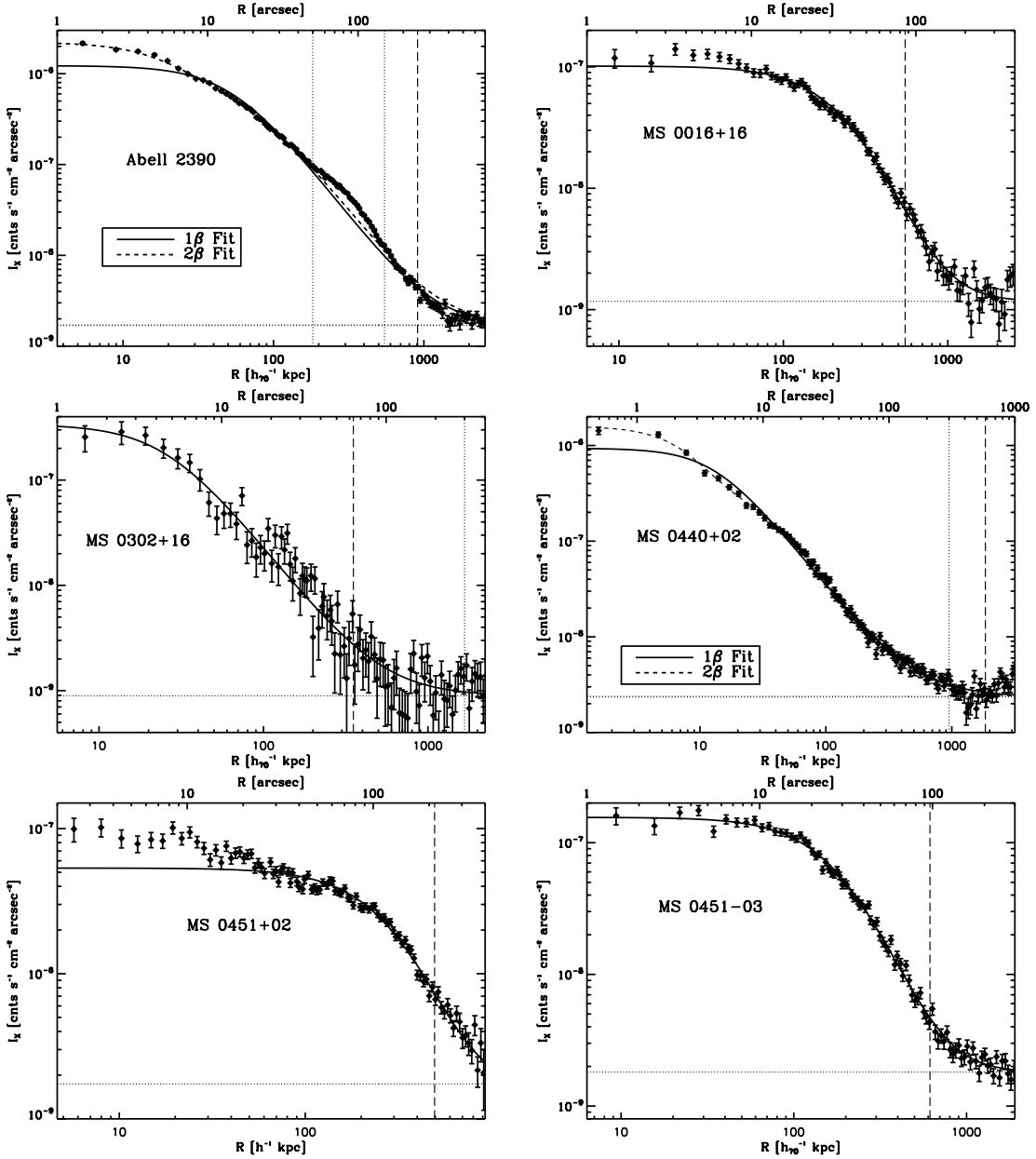


FIG. 2.—Surface brightness profiles. Radial surface brightnesses of CNOX clusters calculated in  $1''$  annular bins using 0.6–7.0 keV data. Horizontal dotted lines denote the best-fitting background of the model. Pairs of vertical dotted lines indicate regions of the profile that were excluded from fitting, while a single vertical dotted line denotes the radius to which fitting was performed. Solid lines describe the best-fitting single- $\beta$  model for each cluster, while short-dashed lines indicate double- $\beta$  model fits to the data. Dashed vertical lines represent  $R_{2500}$ . Cluster emission is well described by either a single- or double- $\beta$  model, except in the case of MS 0451+02, which exhibits a significant amount of substructure. Seemingly high values of reduced  $\chi^2$  are a consequence of fitting high-resolution data with small error bars, such that even small deviations from symmetry will drive  $\chi^2$  up significantly.

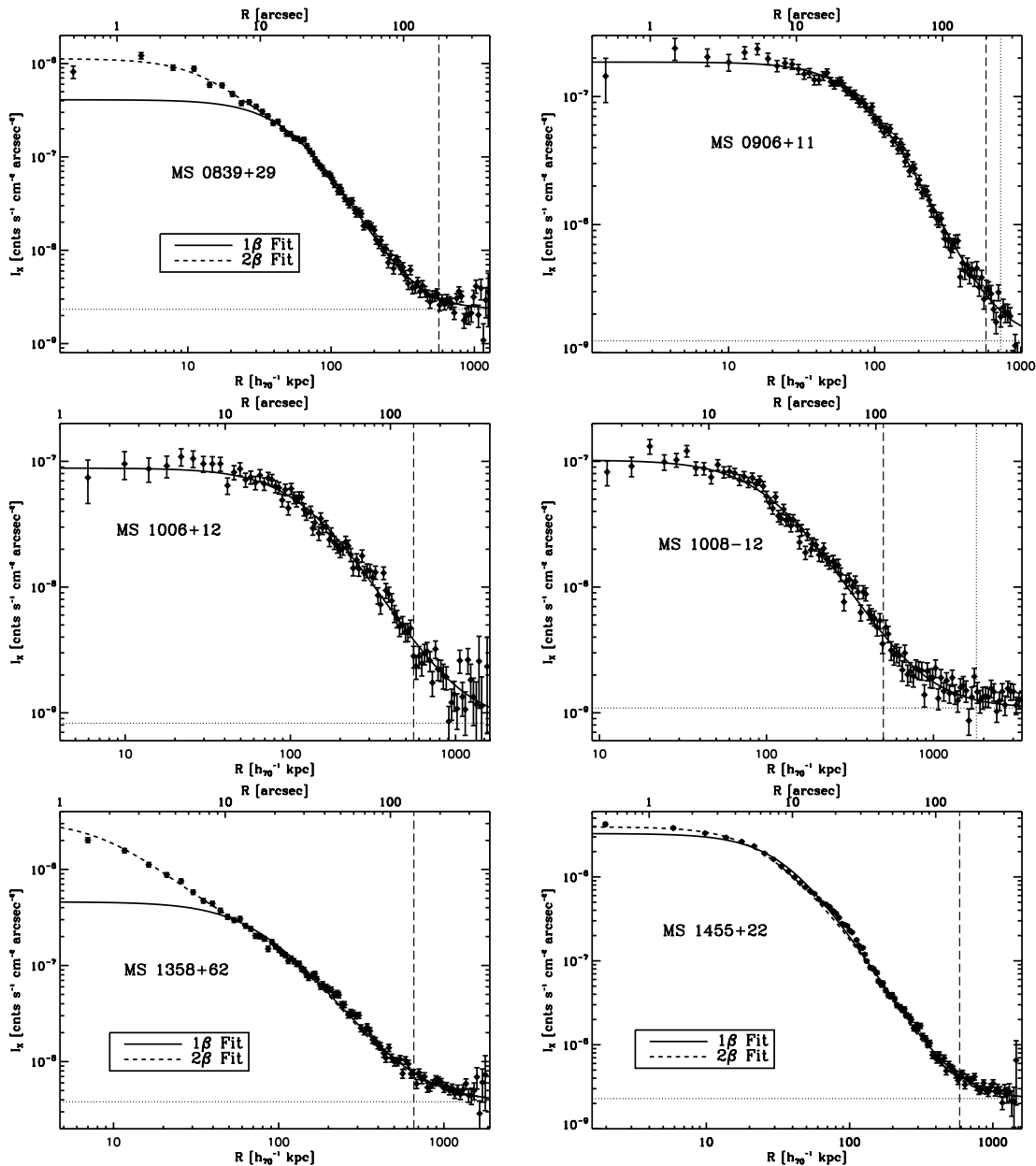


FIG. 2.—Continued

radius. These spectra were then analyzed with XSPEC 11.3.2 (Arnaud 1996), using weighted response matrices (RMFs) and effective area files (ARFs) generated with the CIAO tool `acis_spec` and the latest version of the *Chandra* calibration database (CALDB 3.0.1). Background spectra were extracted from the aim point chip as far away from the cluster as possible. Each spectrum was grouped to contain at least 20 counts per energy bin.

Spectra were fitted with single-temperature spectral models, inclusive of foreground absorption. Each spectrum was initially fit with the absorbing column frozen at its measured value (Dickey & Lockman 1990), and redshifts were fixed throughout the analysis. Metal abundances were allowed to vary. Data with energies below 0.6 keV and above 7.0 keV were again excluded.

In some cases evidence of excess photoelectric absorption has been seen in cooling flow clusters (Allen & Fabian 1997; Allen 2000). To investigate this possibility, a second fit was performed, allowing the absorbing column to vary. No evidence for excess absorption was found in 13 of the 14 clusters. The MS 0440+02

spectrum, however, was equally well fit by a model inclusive of excess foreground absorption.

The results of these fits, combined with the best-fitting  $\beta$ -model parameters from § 3, were then used to estimate the value of  $R_{2500}$  for each cluster. This is accomplished by combining the equation for total gravitating mass

$$M_{\text{tot}}(<r) = -\frac{T(r)r}{G\mu_p} \left( \frac{\delta \ln \rho}{\delta \ln r} + \frac{\delta \ln T}{\delta \ln r} \right), \quad (3)$$

where  $\mu_p$  is the mean mass per particle, with the definition of mass overdensity,

$$M_{\text{tot}}(r_\Delta) = \frac{4}{3} \pi \rho_c r_\Delta^3 \Delta, \quad (4)$$

where the critical density  $\rho_c = 3H_z^2/8\pi G$ ,  $z$  is the cluster redshift, and  $\Delta$  is the factor by which the density at  $r_\Delta$  exceeds the critical density. These equations are then combined with the

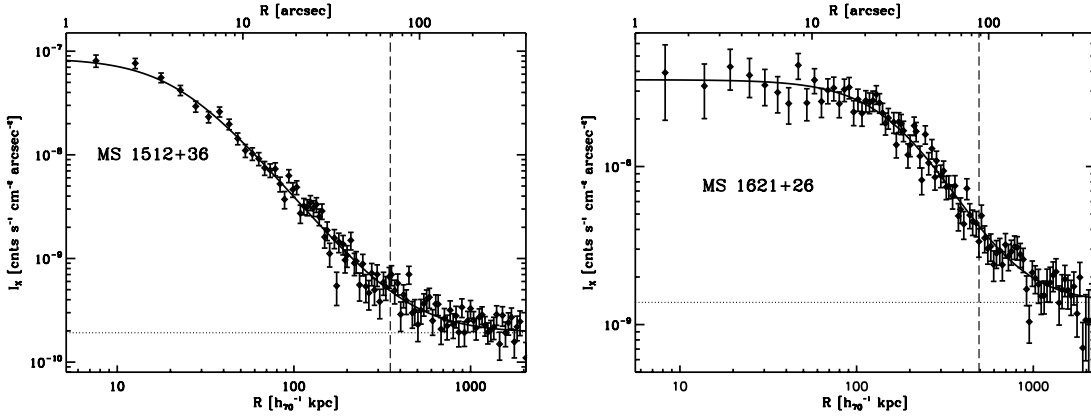


FIG. 2.—Continued

density profile implied from the  $\beta$ -model (assuming hydrostatic equilibrium, spherical symmetry, and isothermality),

$$\rho_{\text{gas}}(r) = \rho_0 \left(1 + \frac{r^2}{r_c^2}\right)^{-3\beta/2}, \quad (5)$$

resulting in the equation (Ettori 2000; Ettori et al. 2004)

$$\frac{r_\Delta}{r_c} = \sqrt{\left[ \frac{3\beta T}{G\mu m_p (4/3)\pi\rho_c(1+z)^3 r_c^2 \Delta} \right]} - 1. \quad (6)$$

After the initial estimation of  $R_{2500}$ , additional spectra were extracted from within that radius, and spectral fitting was performed again. This iterative process was continued until fitted temperatures and calculated values of  $R_{2500}$  were consistent with extraction radii. The results of this process, including values of  $R_{2500}$ , temperatures, and abundances are shown in Table 4, along with 90% confidence ranges.

An additional process was carried out for the five cooling core clusters in our sample. Using spatially resolved temperature profiles (§ 4.2), the radius within which cooling became prominent in each cluster ( $R_{\text{cutoff}}$ ) was estimated. A single annular spectrum was then extracted for each cluster from that radius to  $R_{2500}$  and fitted with single-temperature spectral models. The observation

of MS 0440+02 did not possess enough signal to constrain a fit to the cooling-flow-excised spectrum; therefore, it was discarded. The results of these fits are shown in Table 5, along with inner extraction radii and calculated values of  $R_{2500}$ .

Overall, our integrated temperatures are comparable to the previous *Röntgensatellit* (*ROSAT*) results of Lewis et al. (1999), although they are better constrained through *Chandra* observations. More recent analyses of subsets of these clusters have been conducted with *ROSAT* (Mohr et al. 2000), *ASCA* (Matsumoto et al. 2000; Henry 2004), and *Chandra* (Allen et al. 2001; Arabadjic et al. 2002; Donahue et al. 2003; Ettori & Lombardi 2003; Ettori et al. 2004). Our fitted temperatures are consistent within errors of the vast majority of the values reported in these papers. Noticeable discrepancies arise occasionally in the case of cooling flow clusters (in which some of these authors have not excised the cooling flow contribution to integrated temperature) and MS 1008–1224, for which we consistently derive a lower temperature than other studies. This is not surprising considering the irregular morphology of this cluster, and may be due to differences in the regions for which spectra were extracted. Metallicities for this sample are consistent with an overall value of  $\sim 0.3$  solar, as is seen in lower redshift clusters. This suggests that ICM enrichment occurs early in a cluster's history, evidence that is corroborated by the work of Mushotzky & Loewenstein (1997).

TABLE 4  
SINGLE-TEMPERATURE SPECTRAL FITS FOR  $R < R_{2500}$

Cluster	$R_{2500}$ ( $h_{70}^{-1}$ kpc)	$kT$ (keV)	$N_{\text{H}}$ ( $10^{20}$ $\text{cm}^{-2}$ )	$Z$ ( $Z_{\odot}$ )	$\chi^2/\text{DOF}$
Abell 2390 .....	$701^{+25}_{-19}$	$10.3^{+0.6}_{-0.5}$	6.8	$0.4 \pm 0.1$	401.8/434
MS 0015.9+1609 .....	$550^{+38}_{-35}$	$9.2^{+1.0}_{-0.9}$	4.07	$0.3 \pm 0.1$	185.5/271
MS 0302.7+1658 .....	$352^{+139}_{-72}$	$4^{+3}_{-1}$	10.9	$0.1^{+1}_{-0.1}$	10.3/26
MS 0440.5+0204 .....	$640^{+120}_{-68}$	$8^{+2}_{-1}$	9.67	$0.8^{+0.6}_{-0.5}$	272.2/378
	$583^{+95}_{-66}$	$7 \pm 2$	$12 \pm 3$	$0.8^{+0.5}_{-0.4}$	267.7/377
MS 0451.5+0250 .....	$496^{+90}_{-74}$	$6.1^{+0.7}_{-0.6}$	7.8	$0.4 \pm 0.1$	443.9/420
MS 0451.6–0305 .....	$614^{+48}_{-38}$	$10.2 \pm 1$	5.07	$0.4 \pm 0.1$	223/258
MS 0839.8+2938 .....	$491^{+24}_{-22}$	$4.0 \pm 0.3$	4.11	$0.6 \pm 0.2$	241.7/283
MS 0906.5+1110 .....	$582^{+44}_{-34}$	$5.6^{+0.8}_{-0.6}$	3.54	$0.2 \pm 0.2$	134.2/319
MS 1006.0+1202 .....	$557^{+67}_{-45}$	$7 \pm 1$	3.76	$0.3 \pm 0.2$	100/199
MS 1008.1–1224 .....	$501^{+41}_{-32}$	$5.9^{+0.9}_{-0.7}$	6.98	$0.2 \pm 0.2$	159.5/203
MS 1358.4+6245 .....	$575^{+72}_{-44}$	$8.0^{+1.1}_{-0.9}$	1.93	$0.5 \pm 0.2$	272.2/332
MS 1455.0+2232 .....	$496 \pm 7$	$4.4 \pm 0.1$	3.13	$0.38 \pm 0.05$	569.6/385
MS 1512.4+3647 .....	$351^{+42}_{-32}$	$3.4^{+0.8}_{-0.7}$	1.38	$0.6^{+0.5}_{-0.4}$	43.2/74
MS 1621.5+2640 .....	$493^{+109}_{-68}$	$7^{+3}_{-2}$	3.57	$0.4 \pm 0.4$	56.3/116

TABLE 5  
COOLING CORE CORRECTED SINGLE-TEMPERATURE SPECTRAL FITS FOR  $R < R_{2500}$

Cluster	$R_{\text{cutoff}}$ ( $h_{70}^{-1}$ kpc)	$R_{2500}$ ( $h_{70}^{-1}$ kpc)	$kT$ (keV)	$N_{\text{H}}$ ( $10^{20}$ cm $^{-2}$ )	$Z$ ( $Z_{\odot}$ )	$\chi^2/\text{DOF}$
Abell 2390 .....	66	$761_{-30}^{+35}$	$12.1_{-0.9}^{+1}$	6.8	$0.3 \pm 0.3$	355/434
MS 0839.8+2938 .....	109	$565_{-53}^{+72}$	$5 \pm 1$	4.11	$0.6_{-0.4}^{+0.5}$	195.5/237
MS 1358.4+6245 .....	154	$658_{-59}^{+93}$	$9_{-1}^{+2}$	1.93	$0.4 \pm 0.3$	209/253
MS 1455.0+2232 .....	211	$575_{-35}^{+45}$	$5.9_{-0.7}^{+0.9}$	3.13	$0.4 \pm 0.2$	238/273

#### 4.2. Spatially Resolved Spectra

With the goal of elucidating the radial dependence of temperature for the clusters in our sample, spectra were extracted within circular annuli spanning the central  $150\text{--}600 h_{70}^{-1}$  kpc of each

cluster, depending on the signal-to-noise ratio of each observation. The extraction regions were sized to include at least 2500 counts per spectrum in the 0.6–7.0 keV band for each data set. This number was chosen as a minimum for achieving reasonable temperature constraints on the emission in each annulus.

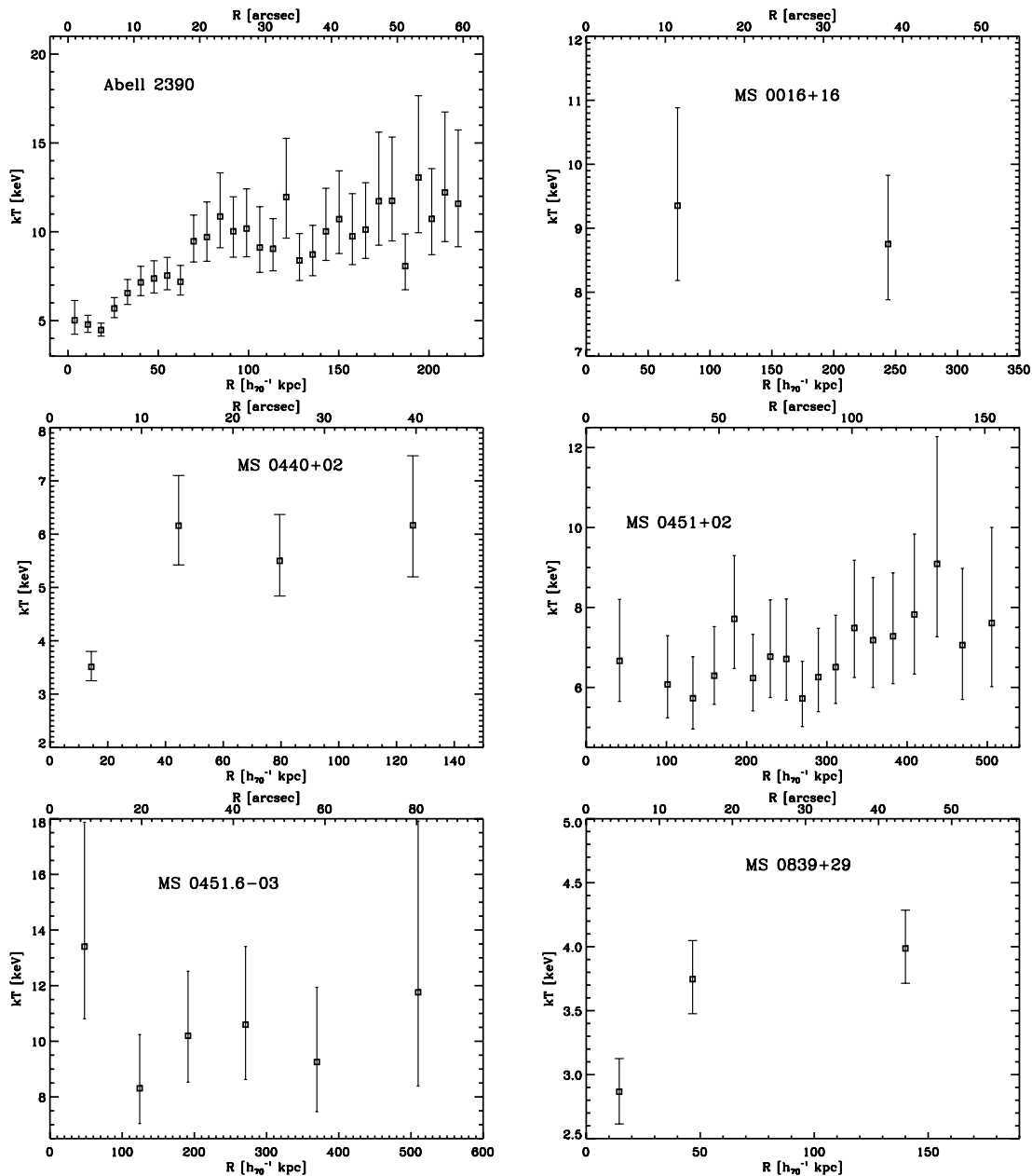
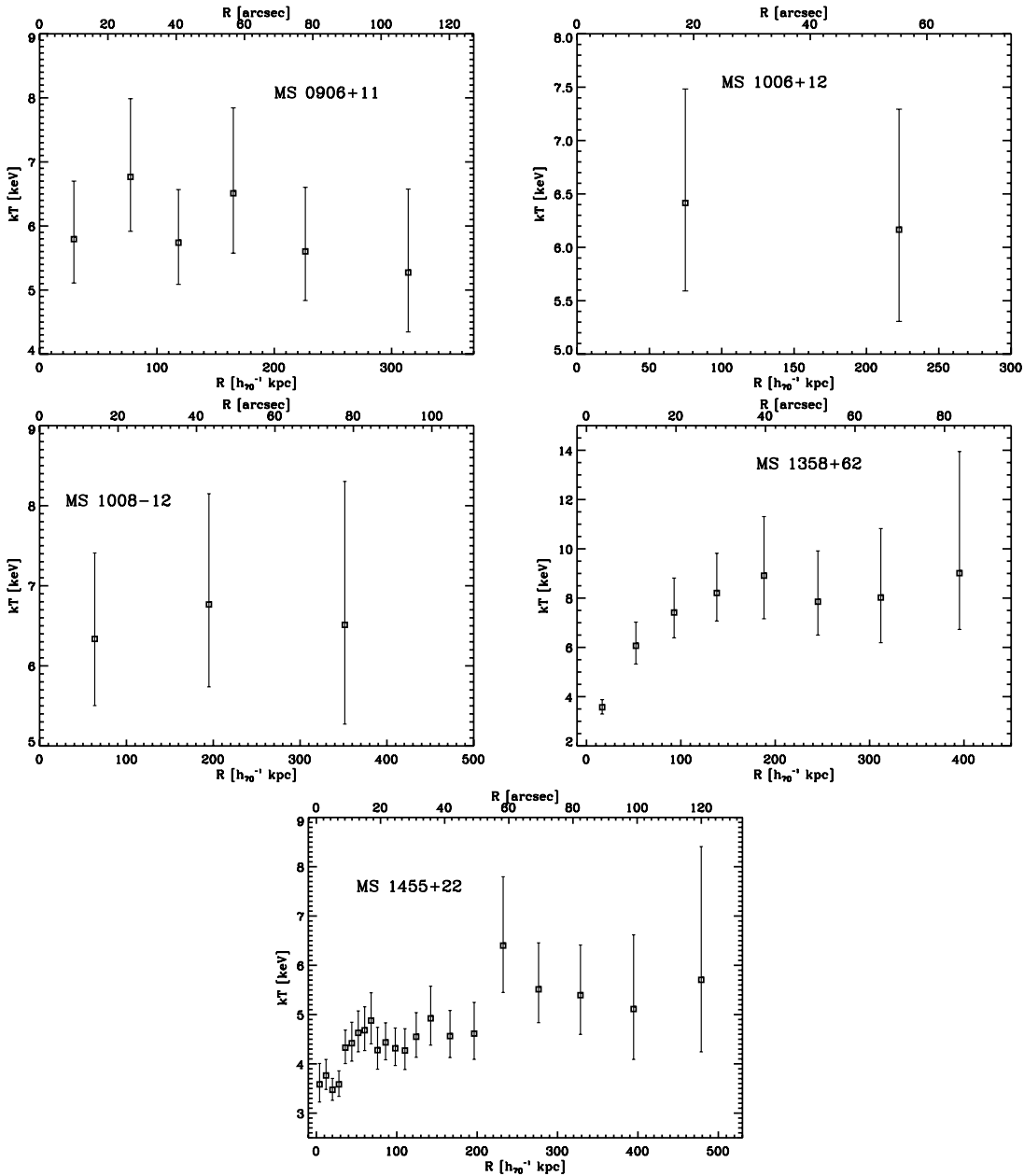


FIG. 3.—Temperature profiles. Radial temperature profiles determined by fitting, in XSPEC, single-temperature spectral models to spectra extracted from circular annuli selected to include a minimum of 2500 counts in the 0.6–7.0 keV band. Error bars represent 90% confidence limits. Indications of cool cores are seen in Abell 2390, MS 0440+02, MS 0839+29, MS 1358+62, and MS 1455+22.

FIG. 3.— *Continued*

Extractions were performed after the removal of previously detected point sources (§ 2), using the CIAO tool *acispec*, which incorporates the changing response over large areas of the detector. Three of the 14 clusters in this sample did not possess enough signal for more than one extraction region, and were removed from the sample during the subsequent spatial analysis. Spectra from the 11 remaining clusters were then grouped to contain 20 counts  $\text{bin}^{-1}$ , and were analyzed using XSPEC. Single-temperature spectral models with fixed galactic absorption and varying abundances were fitted to the data. The results of these fits were used to create a temperature profile for each cluster.

Figure 3 illustrates the 11 resulting temperature profiles. It is clear from these figures that significant cooling cores are present in five of the clusters in this sample: Abell 2390, MS 0440+02, MS 0839+29, MS 1358+62, and MS 1455+22. These are the same five clusters that required double- $\beta$  model fits to their surface brightness profiles (§ 3). The remaining six temperature profiles are consistent with isothermality.

#### 4.3. The Universal Temperature Profile

The spatially resolved temperature profiles of the five cooling core clusters were scaled by  $R_{2500}$  and  $T_{2500}$  in an attempt to check their consistency with the universal temperature profile proposed by Allen et al. (2001). The combined data from these five clusters were then fit using the functional form

$$\frac{T(R)}{T_{2500}} = T_0 + T_1 \left[ \frac{(x/x_c)^\eta}{1 + (x/x_c)^\eta} \right],$$

with  $x = R/R_{2500}$  (Allen et al. 2001). This fit resulted in  $T_0 = 0.397 \pm 0.007$ ,  $T_1 = 0.56 \pm 0.02$ ,  $x_c = 0.0865 \pm 0.0002$ , and  $\eta = 1.3 \pm 0.2$ , with a reduced  $\chi^2$  of 1.3.

These values are all consistent with the best fit found by Allen et al. (2001). The resulting function, however, does not asymptotically approach 1 at large radii, ostensibly due to the fact that these temperature profiles do not extend all the way to  $R_{2500}$ .

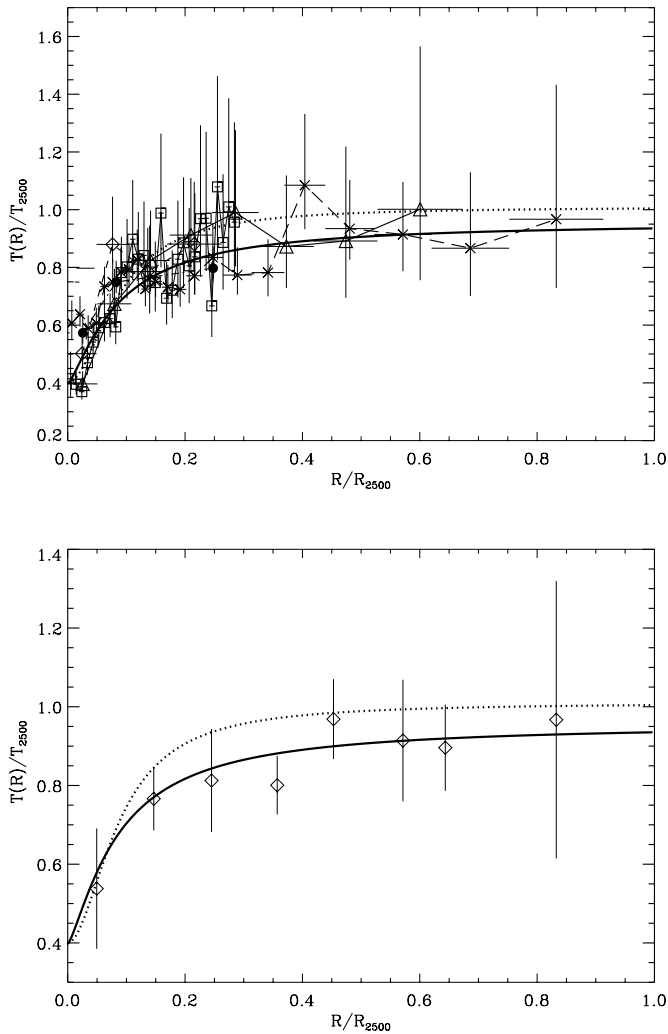


FIG. 4.— Universal temperature profiles. *Top*: Individual temperature profiles of the five cooling core clusters in this sample. *Squares and solid line*: Abell 2390; *diamonds and dashed line*: MS 0440+02; *Circles and dot-dashed line*: MS 0839+29; *triangles and triple-dot-dashed line*: MS 1358+62; *crosses and long-dashed line*: MS 455+22. The best fit to the data is overlaid as a thick solid line, while the dotted line indicates the best fit found by Allen et al. (2001). *Bottom*: Weighted average temperature profile of the combined five clusters in  $0.1R/R_{2500}$  bins, with best-fitting models overlaid as described above.

Figure 4 shows the individual temperature profiles as well as the binned and averaged temperature profile of the five clusters, with the best-fitting functions overlaid.

## 5. MASS DETERMINATIONS

Using the results of the spectral fits and  $\beta$ -model fits, along with equations (3), (5), and (6), gas masses and total masses were calculated out to both  $R_{2500}$  and  $R_{200}$  for the clusters in our sample. Central densities were determined via an expression relating the observable cluster X-ray luminosity to gas density, using emission measures obtained during spectral fitting in XSPEC.

For the nine noncooling core clusters, single-temperature spectra fits and single- $\beta$  model parameters were used. For the five clusters that exhibit significant cooling, spectral parameters from cooling-core-excised spectral fits were used, and  $\beta$  and  $r_c$  were taken from the results of double- $\beta$  model fits.

To determine the effects of inner temperature gradients on total cluster mass, least-squares fitting was performed on the temperature profiles obtained in § 4.2 for the five cooling core clusters. The resulting parameterizations were included in equation (3), and

TABLE 6  
MASS ESTIMATES FOR  $R < R_{2500}$

Cluster	$n_0$ ( $10^{-1} \text{ cm}^{-3}$ )	$M_{\text{gas}}$ ( $10^{13} h_{70}^{-1} M_{\odot}$ )	$M_{2500}$ ( $10^{13} h_{70}^{-1} M_{\odot}$ )
Abell 2390 .....	$0.165 \pm 0.004$	$4.5^{+0.2}_{-0.3}$	$59 \pm 3$
MS 0015.9+1609 .....	$0.0498^{+0.001}_{-0.0004}$	$2.38 \pm 0.08$	$38 \pm 3$
MS 0302.7+1658 .....	$0.271 \pm 0.008$	$0.49 \pm 0.06$	$9 \pm 3$
MS 0440.5+0204 .....	$0.214 \pm 0.003$	$1.24 \pm 0.07$	$26^{+4}_{-5}$
MS 0451.5+0250 .....	$0.0259 \pm 0.0003$	$2.1 \pm 0.1$	$17.6 \pm 0.9$
MS 0451.6–0305 .....	$0.0694 \pm 0.0005$	$2.71^{+0.08}_{-0.09}$	$52 \pm 4$
MS 0839.8+2938 .....	$0.184 \pm 0.004$	$1.2 \pm 0.1$	$23 \pm 3$
MS 0906.5+1110 .....	$0.0972^{+0.0009}_{-0.001}$	$1.58 \pm 0.07$	$24 \pm 2$
MS 1006.0+1202 .....	$0.0558^{+0.0008}_{-0.0009}$	$1.6 \pm 0.1$	$25 \pm 3$
MS 1008.1–1224 .....	$0.0670 \pm 0.0008$	$1.34 \pm 0.07$	$19 \pm 2$
MS 1358.4+6245 .....	$0.091 \pm 0.003$	$2.2 \pm 0.3$	$47 \pm 6$
MS 1455.0+2232 .....	$0.353 \pm 0.009$	$1.9 \pm 0.2$	$27 \pm 2$
MS 1512.4+3647 .....	$0.143 \pm 0.003$	$0.19 \pm 0.02$	$7 \pm 1$
MS 1621.5+2640 .....	$0.0304 \pm 0.0006^+$	$1.1 \pm 0.1$	$24 \pm 5$

masses were calculated out to the edge of the cooling region (Table 5). Masses were also calculated without the inclusion of this parameterization, and the results compared. According to the outcome of this exercise, the inclusion of temperature gradients in mass calculations of the five cooling core clusters in our sample would result in, at most, a 0.3% correction to the total mass within the cooling region. This correction is negligible compared to the other uncertainties in mass calculations and is therefore not included in the final results.

An additional uncertainty is present in mass estimations of MS 0451+0250 due to its significant irregularity. Choosing a centroid at the center of the extended emission rather than one at the most central peak of emission produces a total mass that is greater by 25%. The  $\beta$ -parameter that results from using this centroid, however, is unusually high (1.9). X-ray mass determinations are presented in Tables 6 and 7 along with 68% confidence intervals.

## 6. GAS MASS FRACTIONS AND $\Omega_m$

Under the assumption that clusters provide a fair representation of the universe, gas mass fractions,  $f_{\text{gas}}$ , defined as the ratio of cluster gas mass to total gravitating mass, were calculated for our sample within  $R_{200}$  and are listed in Table 7. The  $f_{\text{gas}}$  values can be used to calculate the cosmological mass density,  $\Omega_m$ , via the relation

$$\Omega_m = \frac{\Omega_b}{f_{\text{gas}}(1 + 0.19 h^{0.5})}, \quad (7)$$

(Allen et al. 2002), where  $0.19 h^{0.5}$  represents the baryonic contribution from optically luminous matter (White et al. 1993; Fukugita et al. 1998). A value of  $\Omega_b h^2$  of  $0.0223^{+0.0007}_{-0.0009}$  is adopted (Wilkinson Microwave Anisotropy Probe [WMAP]; Spergel et al. 2006), and here, we take  $h = 0.71$ . Using an average  $f_{\text{gas}} = 0.092 \pm 0.004 h_{70}^{-3/2}$  within  $R_{200}$  for our sample, we calculate a cosmological mass density of  $\Omega_m = 0.42 \pm 0.02$  (68% confidence, with error bars representing the formal error). This value is higher than WMAP 3 yr results (Spergel et al. 2006), suggesting an overall lower than average gas mass fraction for this sample.

## 7. MASS COMPARISONS

### 7.1. Dynamical Mass Comparisons

Comparisons between X-ray and dynamical masses for the CNOC sample were previously undertaken by Lewis et al. (1999) using ROSAT observations. While they found good agreement

TABLE 7  
MASS ESTIMATES FOR  $R < R_{200}$

Cluster	$R_{200}^a$ ( $h_{70}^{-1}$ Mpc)	$M_{\text{gas}}$ ( $10^{14} h_{70}^{-1} M_{\odot}$ )	$M_{200}$ ( $10^{14} h_{70}^{-1} M_{\odot}$ )	$f_{\text{gas}}$ ( $h_{70}^{3/2}$ )
Abell 2390 .....	$2.7 \pm 0.1$	$2.9 \pm 0.2$	$21 \pm 1$	$0.14 \pm 0.01$
MS 0015.9+1609 .....	$2.1 \pm 0.1$	$1.36 \pm 0.05$	$17 \pm 1$	$0.079 \pm 0.006$
MS 0302.7+1658 .....	$1.2^{+0.5}_{-0.3}$	$0.33 \pm 0.04$	$3 \pm 1$	$0.10^{+0.03}_{-0.04}$
MS 0440.5+0204 .....	$2.1^{+0.3}_{-0.2}$	$0.87 \pm 0.05$	$9 \pm 2$	$0.10 \pm 0.02$
MS 0451.5+0250 .....	$2.5^{+0.2}_{-0.1}$	$2.1 \pm 0.2$	$15.9 \pm 0.8$	$0.13 \pm 0.01$
MS 0451.6-0305 .....	$2.3^{+0.2}_{-0.1}$	$1.22 \pm 0.05$	$21 \pm 2$	$0.058 \pm 0.005$
MS 0839.8+2938 .....	$2.0^{+0.3}_{-0.2}$	$0.56 \pm 0.05$	$8 \pm 1$	$0.07 \pm 0.01$
MS 0906.5+1110 .....	$2.1^{+0.2}_{-0.1}$	$0.83 \pm 0.04$	$8.6 \pm 0.7$	$0.096^{+0.009}_{-0.01}$
MS 1006.0+1202 .....	$2.0 \pm 0.2$	$1.11 \pm 0.08$	$9 \pm 1$	$0.12 \pm 0.02$
MS 1008.1-1224 .....	$1.8 \pm 0.1$	$0.90 \pm 0.05$	$7.2 \pm 0.6$	$0.12 \pm 0.01$
MS 1358.4+6245 .....	$2.4^{+0.3}_{-0.2}$	$1.1 \pm 0.2$	$17 \pm 2$	$0.06 \pm 0.01$
MS 1455.0+2232 .....	$2.04^{+0.2}_{-0.1}$	$0.83 \pm 0.08$	$9.5 \pm 0.9$	$0.09 \pm 0.01$
MS 1512.4+3647 .....	$1.3 \pm 0.1$	$0.13 \pm 0.01$	$2.7^{+0.3}_{-0.4}$	$0.047 \pm 0.007$
MS 1621.5+2640 .....	$1.8^{+0.4}_{-0.2}$	$0.86 \pm 0.08$	$10 \pm 2$	$0.09 \pm 0.02$

<sup>a</sup> 90% confidence intervals.

between the two methods of mass estimation, accurate surface brightness modeling and detailed investigations of cluster temperature gradients were unavailable due to the comparatively poor spatial resolution of *ROSAT* (particularly at moderate redshift). Here, we use the 0".5 spatial resolution of *Chandra* to improve the accuracy of these initial comparisons.

Detailed dynamical studies of CNOC clusters were performed by Carlberg et al. (1996), Borgani et al. (1999), and Van der Marel et al. (2000). Carlberg et al. (1996) provides velocity dispersions obtained from CFHT spectroscopy, Borgani et al. (1999) adjusts these values by employing an improved interloper-removal algorithm, and Van der Marel et al. (2000) investigates the isotropicity and galaxy distribution of a composite CNOC cluster created via dimensionless scaling. Here, we primarily draw from the work of Borgani et al. (1999) and Van der Marel et al. (2000) for our mass estimates.

Dynamical masses can be calculated from velocity dispersions via the Jeans equation

$$M(r) = \frac{-\sigma_r^2 r}{G} \left[ \frac{\delta \ln \sigma_r^2}{\delta \ln r} + \frac{\delta \ln \nu(r)}{\delta \ln r} + 2\beta \right], \quad (8)$$

where  $\sigma_r$  represents the radial velocity dispersion,  $\nu(r)$  is the galaxy number density profile, and  $\beta$  represents the anisotropy of the system. According to Van der Marel et al. (2000), the CNOC clusters can be treated as isotropic (i.e.,  $\beta = 0$ ), and  $\nu(r)$  takes the form

$$\nu(r) = \nu_0 (r/a)^{-\gamma} (1 + r/a)^{\gamma-3}, \quad (9)$$

where the length scale of the mass distribution is set by the parameter  $a$ , and  $\gamma$  represents the logarithmic power-law slope near the center. The best-fitting values of  $a$  and  $\gamma$  for isotropicity are 0.224 and 0.75, respectively. This relationship was obtained by creating a composite CNOC cluster via dimensionless scaling (Van der Marel et al. 2000), as was a plot of  $\sigma$  versus  $r$ . Figure 2 of Van der Marel et al. (2000) indicates that  $\sigma$  is not a strong function of radius out to  $R_{200}$ , and in keeping with both Lewis et al. (1999) and Carlberg et al. (1996), we assume that  $\sigma(r) = \sigma$ .

Using equation (8) and the velocity dispersions of Borgani et al. (1999), dynamical masses were calculated for our sample out to  $R_{200}$  (as determined by X-ray parameters in § 4.1). These masses were then compared to X-ray-derived masses from § 5). A weighted average gives an overall dynamical to X-ray mass ratio of 0.97  $\pm$

0.05, where the error bar indicates the uncertainty in the mean. Table 8 lists both dynamical and X-ray-derived masses along with their ratio and 68% confidence intervals. Figure 5 is a plot indicating the dynamical to X-ray mass ratio of each cluster in the sample.

The high dynamical to X-ray mass ratios of MS 1006.0+1202 and MS 1008.1-1224 may be due to overestimated velocity dispersions of these objects, as they both have markedly irregular emission (Fig. 1). However, we also see evidence of good agreement between X-ray and dynamical masses in irregular objects (MS 0451.5+0250), as well as disagreement in some regular objects (MS 0839.8+2938); therefore, a clear pattern does not make itself evident. Likewise, cooling core objects show no obvious systematic departures from consistency. Overall, dynamical and X-ray mass estimations for this sample show remarkable agreement.

Our resulting ratio of dynamical to X-ray masses is consistent with that quoted by Lewis et al. (1999) in their *ROSAT* study, however the scatter about the mean of our distribution is  $\sim 5\%$  smaller. This decrease in scatter is indicative of the improved spatial and spectral resolution of *Chandra*. In addition, Lewis et al. (1999) systematically overestimate the core radii of cooling flow clusters and, therefore, their masses, another result that is likely due to the poorer spatial resolution of *ROSAT*.

TABLE 8  
DYNAMICAL MASS COMPARISONS FOR  $R < R_{200}$

Cluster	Dynamical Mass ( $10^{14} h_{70}^{-1} M_{\odot}$ )	X-Ray Mass ( $10^{14} h_{70}^{-1} M_{\odot}$ )	Ratio (Dynamical/X-Ray)
Abell 2390 .....	$26^{+4}_{-3}$	$21 \pm 1$	$1.2 \pm 0.2$
MS 0015.9+1609 .....	$16^{+5}_{-3}$	$17 \pm 1$	$0.9^{+0.3}_{-0.2}$
MS 0302.7+1658 .....	$3.8^{+1}_{-0.6}$	$3 \pm 1$	$1.3 \pm 0.5$
MS 0440.5+0204 .....	$6^{+2}_{-1}$	$9 \pm 2$	$0.7^{+0.3}_{-0.2}$
MS 0451.5+0250 .....	$15 \pm 2$	$15.9 \pm 0.8$	$0.9 \pm 0.1$
MS 0451.6-0305 .....	$24^{+4}_{-3}$	$21 \pm 2$	$1.1 \pm 0.2$
MS 0839.8+2938 .....	$12 \pm 3$	$8 \pm 1$	$1.5 \pm 0.4$
MS 0906.5+1110 .....	$8^{+2}_{-1}$	$8.6 \pm 0.7$	$0.9^{+0.2}_{-0.1}$
MS 1006.0+1202 .....	$13^{+4}_{-3}$	$9 \pm 1$	$1.4^{+0.5}_{-0.4}$
MS 1008.1-1224 .....	$12^{+3}_{-2}$	$7.2 \pm 0.6$	$1.7^{+0.4}_{-0.3}$
MS 1358.4+6245 .....	$14^{+2}_{-1}$	$17 \pm 2$	$0.8^{+0.2}_{-0.1}$
MS 1455.0+2232 .....	$12^{+3}_{-2}$	$9.5 \pm 0.9$	$1.3^{+0.3}_{-0.2}$
MS 1512.4+3647 .....	$2.6^{+1}_{-0.8}$	$2.7^{+0.3}_{-0.4}$	$1.0^{+0.4}_{-0.3}$
MS 1621.5+2640 .....	$8 \pm 1$	$10 \pm 2$	$0.8 \pm 0.2$

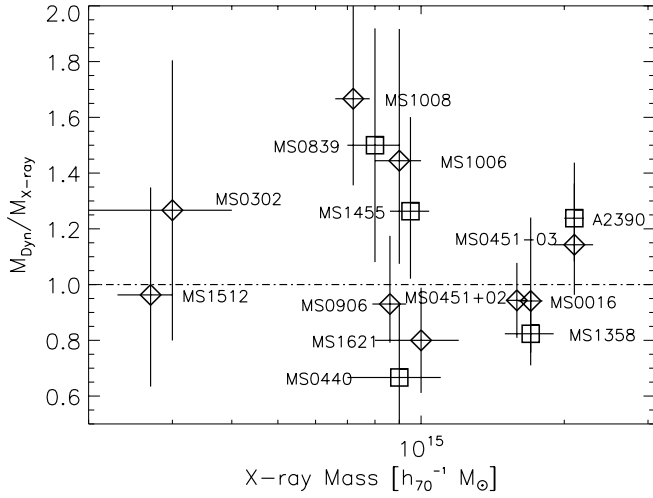


FIG. 5.—Dynamical vs. X-ray masses. X-ray mass estimates are plotted against the ratio  $M_{\text{dyn}}/M_X$ . The dot-dashed line indicates a mass ratio of 1.0. Squares represent cooling core clusters. Error bars denote 68% confidence limits.

### 7.2. Weak-lensing Mass Comparisons

Weak-lensing mass estimates were obtained for seven of the clusters in our sample using deep optical observations at the CFHT 3.6 m telescope (H. Hoekstra 2006, in preparation). The model-independent projected mass estimates that we employ in this paper were calculated for the inner  $500 h^{-1}$  kpc of each cluster, using a cosmology of  $H_0 = 100$ ,  $\Omega_m = 0.3$ , and  $\Omega_\Lambda = 0.7$ .

To compare X-ray-derived masses to weak-lensing masses, we calculated a cylindrical X-ray mass within  $500 h^{-1}$  kpc. This was done using previously determined  $\beta$ -models, the adopted cosmology (see above), and a cylindrical mass projection out to 10 Mpc from the cluster core. A comparison of weak-lensing masses to X-ray-derived masses can be found in Table 9; a plot of mass ratios is given in Figure 6. Contributions to lensing signal from structures along the line of sight may result in masses that are biased somewhat high. Similarly, large-scale structure along the line of sight results in increased scatter (Hoekstra 2001). Despite these possible challenges, the weighted average of our mass ratios gives a weak-lensing to X-ray mass ratio of  $0.99 \pm 0.08$ , with a reduced  $\chi^2$  of 0.93. Although the distribution in Figure 6 appears asymmetric, it is not statistically significant.

## 8. X-RAY SCALING LAWS

### 8.1. The $L_X$ - $T_X$ Relationship

Unabsorbed bolometric X-ray luminosities within  $R_{2500}$  were obtained for our sample in the following manner. Unabsorbed X-ray luminosities for the 2–10 keV band were calculated in

TABLE 9  
WEAK-LENSING MASS COMPARISONS FOR  $R < 500 h^{-1}$  kpc

Cluster	Weak-lensing Mass ( $10^{14} h^{-1} M_\odot$ )	X-Ray Mass ( $10^{14} h^{-1} M_\odot$ )	Ratio (Lensing/X-Ray)
Abell 2390 .....	$5.0 \pm 0.6$	$5.3^{+0.5}_{-0.4}$	$0.9 \pm 0.1$
MS 0015.9+1609 .....	$8 \pm 1$	$5.2 \pm 0.4$	$1.5 \pm 0.3$
MS 0906.5+1110 .....	$3.5 \pm 0.7$	$2.8 \pm 0.2$	$1.2 \pm 0.3$
MS 1358.4+6245 .....	$4.2 \pm 0.8$	$4.9 \pm 0.6$	$0.9 \pm 0.2$
MS 1455.0+2232 .....	$3.2 \pm 0.7$	$3.2 \pm 0.3$	$1.0 \pm 0.2$
MS 1512.4+3647 .....	$2.0 \pm 0.8$	$1.4 \pm 0.2$	$1.4 \pm 0.6$
MS 1621.5+2640 .....	$5 \pm 1$	$3.6 \pm 0.7$	$1.4 \pm 0.4$

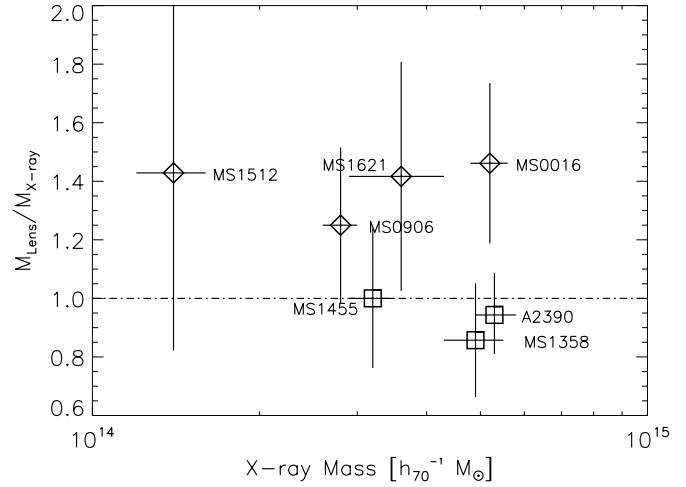


FIG. 6.—Weak lensing vs. X-ray masses. X-ray mass estimates are plotted against the ratio  $M_{\text{lens}}/M_X$ . The dot-dashed line represents a mass ratio of 1.0. Squares indicate cooling core clusters, and error bars denote 68% confidence limits. Although the distribution appears asymmetric, it is not statistically significant.

XSPEC during spectral fitting (§ 4.1). In the case of the five clusters that exhibit significant cooling, corrected and integrated luminosities were obtained by fixing X-ray temperatures at the values determined for cooling-core-corrected spectra (Table 5). To convert 2–10 keV luminosities to bolometric X-ray luminosities, correction factors were obtained via NASA’s Portable, Interactive Multi-Mission Simulator (PIMMS) for each individual cluster, using a thermal bremsstrahlung model and the spectrally determined temperature of the cluster. The resulting bolometric luminosities are given in Table 10.

The  $L_X$ - $T_X$  data were fit using the bivariate correlated errors and intrinsic scatter (BCES) estimator of Akritas & Bershady (1996). This estimator allows for measurement errors in both variables as well as possible intrinsic scatter and was used in both Allen et al. (2001) and Yee & Ellingson (2003). To correct for cosmological effects, a form similar to Allen et al. (2001) was adopted,

$$\frac{L_{2500}}{10^{44} \text{ ergs s}^{-1} E(z)} = C_1 (kT_{2500})^{C_2}, \quad (10)$$

TABLE 10  
CLUSTER RICHNESS AND LUMINOSITY

Cluster	$L_X^a$ ( $10^{44} \text{ ergs s}^{-1}$ )	$B_{\text{gc, red}}$ ( $\text{Mpc}^{1.77}$ )
Abell 2390 .....	$56.1^{+0.2b}_{-0.2}$	$1473 \pm 218$
MS 0015.9+1609 .....	$41.0^{+0.7}_{-1}$	$1789 \pm 260$
MS 0302.7+1658 .....	$5^{+1}_{-1}$	$762 \pm 201$
MS 0440.5+0204 .....	$6.2 \pm 0.2$	$559 \pm 154$
MS 0451.5+0250 .....	$15.0^{+0.3}_{-0.5}$	$1198 \pm 208$
MS 0451.6–0305 .....	$49.1^{+0.9}_{-1}$	$1232 \pm 180$
MS 0839.8+2938 .....	$5.97^{+0.1}_{-0.08} b$	$1106 \pm 187$
MS 0906.5+1110 .....	$8.5 \pm 0.3$	$1134 \pm 209$
MS 1006.0+1202 .....	$9.2 \pm 0.6$	$1330 \pm 216$
MS 1008.1–1224 .....	$9.0^{+0.3}_{-0.5}$	$1444 \pm 212$
MS 1358.4+6245 .....	$17.7^{+0.2b}_{-0.2}$	$1182 \pm 205$
MS 1455.0+2232 .....	$23.2^{+0.1b}_{-0.2}$	$518 \pm 154$
MS 1512.4+3647 .....	$4.9^{+0.4}_{-0.8}$	$582 \pm 180$
MS 1621.5+2640 .....	$8.7^{+0.5}_{-0.8}$	$996 \pm 199$

<sup>a</sup> Unabsorbed bolometric X-ray luminosity for  $R < R_{2500}$ .

<sup>b</sup> Values are cooling core corrected.

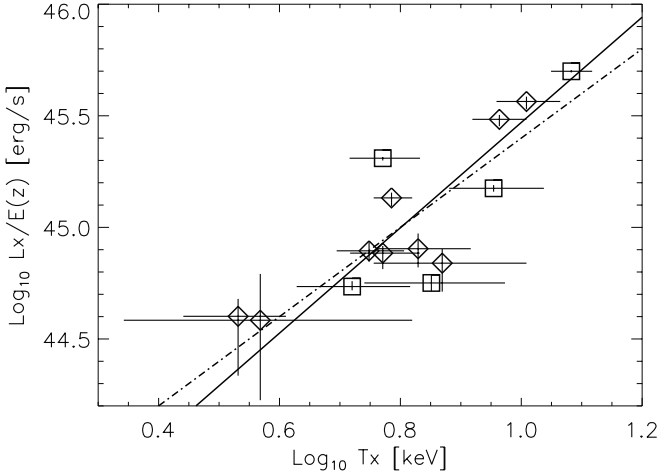


FIG. 7.—The  $L_X$ - $T_X$  relationship. X-ray temperatures are plotted against cosmologically corrected unabsorbed bolometric luminosities within  $R_{2500}$ . Squares represent clusters with cool cores. The solid line indicates the best-fitting relationship, with a slope of  $2.4 \pm 0.2$ . The dot-dashed line illustrates a slope of 2.0. Error bars indicate 90% confidence limits.

where  $E(z) = H_z/H_0 = [\Omega_m(1+z)^3 + \Omega_\Lambda]^{1/2}$ . The best-fitting values were  $C_1 = 0.13^{+0.08}_{-0.05}$  and  $C_2 = 2.4 \pm 0.2$ . While this slope is lower than some estimates (e.g., Arnaud & Evrard 1999; Ettori et al. 2004), it is consistent with both Allen et al. (2001) and Ettori et al. (2002). Because it is steeper than the expected self-similar slope of 2 (Voit 2005), it indicates modest negative evolution in the  $L_X$ - $T_X$  relationship at  $z \sim 0.3$ .

Ettori et al. (2004) examine scaling laws in clusters at moderate to high redshift ( $0.4 < z < 1.3$ ), so here we adopt their definition of scatter for comparison,

$$\sigma_Y \equiv \left[ \sum_{j=1, N} (\log L_{j, \text{obs}} - \log L_{j, \text{pred}})^2 / N \right]^{1/2}.$$

Defined this way, our scatter in luminosity  $\sigma_Y = 0.20$ , is smaller than that of Ettori et al. ( $\sigma_Y = 0.35$ ); however, they have included significantly higher redshift clusters in their fit. A plot of the data with our relationship overlaid is presented in Figure 7.

### 8.2. The Mass- $T_X$ Relationship

A BCES fit was also performed between cluster temperatures and mass estimates. This relationship takes the form (Ettori et al. 2004)

$$E(z)M_{\text{tot}} = C_1(kT)^{C_2}. \quad (11)$$

We again use cluster properties that were determined within  $R_{2500}$ . The best-fitting values were  $C_1 = (1.3^{+0.3}_{-0.2}) \times 10^{13}$  and  $C_2 = 1.7 \pm 0.1$ . This slope is consistent with Allen et al. (2001) and Ettori et al. (2002, 2004) and is again steeper than the expected slope of 1.5 (Voit 2005). Our scatter in mass is also lower than Ettori et al. (2004;  $\sigma_Y = 0.07$  compared to  $\sigma_Y = 0.15$ ). A plot of the data with our relationship overlaid is presented in Figure 8.

### 9. X-ray Properties and Optical Richness

Optical richness is in essence a measurement of the galaxy excess in the direction of a cluster above a certain magnitude limit and within a specific aperture. The particular optical richness parameter that is used in this work,  $B_{\text{gc}}$ , is defined as the amplitude

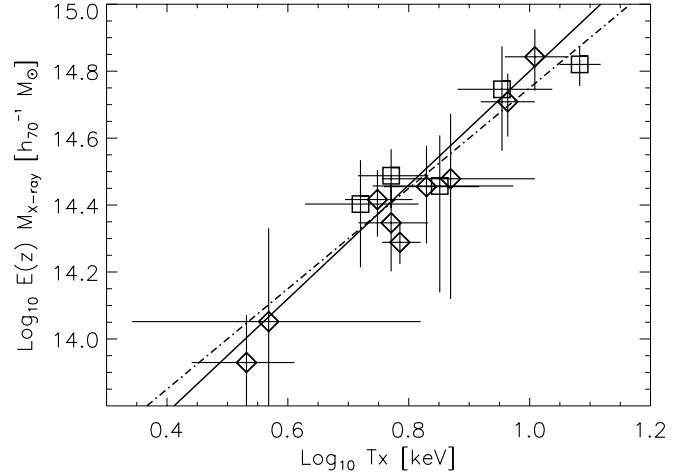


FIG. 8.—The  $M$ - $T_X$  relationship. X-ray temperatures are plotted against X-ray-derived masses within  $R_{2500}$ . Squares represent clusters with cool cores. The solid line indicates the best fitting relationship, with a slope of  $1.7 \pm 0.1$ , while the dot-dashed line represents a slope of 1.5. Error bars indicate 90% confidence limits.

of the galaxy-cluster correlation function (Longair & Seldner 1979),

$$\xi(r) = \left( \frac{r}{r_0} \right)^{-\gamma} = B_{\text{gc}} r^{-\gamma}. \quad (12)$$

Galaxies are observed as projections on the sky; therefore, what is measured is the angular two-point correlation function of galaxies,  $\omega(\theta)$ , where  $\theta$  is the angle on the sky. The function  $\omega(\theta)$  is approximated by a power-law of the form (Davis & Peebles 1983; Yee & Lopez-Cruz 1999)

$$\omega(\theta) = A_{\text{gg}} \theta^{1-\gamma}, \quad (13)$$

where  $A_{\text{gg}}$  is the galaxy-galaxy angular correlation amplitude;  $\omega_\theta$  is taken as the distribution of galaxies around the center of the cluster, and the amplitude is then relabeled as  $A_{\text{gc}}$ . This amplitude can be measured from an image by counting the background-corrected excess of galaxies within a certain  $\theta$  to a particular magnitude limit.

The  $B_{\text{gc}}$  is then calculated through a deprojection analysis that assumes spherical symmetry (Longair & Seldner 1979),

$$B_{\text{gc}} = N_{\text{bg}} \frac{D^{\gamma-3} A_{\text{gc}}}{I_\gamma \Phi[M(m_0, z)]}, \quad (14)$$

where  $N_{\text{bg}}$  represents the background galaxy counts to apparent magnitude  $m_0$ ,  $D$  is the angular diameter distance to the cluster redshift  $z$ ,  $I_\gamma$  is an integration constant, and  $\Phi[M(m_0, z)]$  is the integrated luminosity function of galaxies to the absolute magnitude  $M$  that corresponds to  $m_0$  at  $z$ .

One of the challenges in the calculation of  $B_{\text{gc}}$  involves the lack of a complete knowledge of the galaxy luminosity function at high redshifts. This uncertainty can be minimized by employing the parameter  $B_{\text{gc, red}}$  (Gladders & Yee 2005), which is calculated using galaxies in the red sequence. This parameter is expected to provide a more robust indication of cluster mass due to the well-understood passive evolution of red-sequence cluster galaxies (van Dokkum et al. 1998) as opposed to the more unpredictable nature of star-forming populations. Since one of our main goals in this work is to provide a comparison sample for future studies of clusters at higher redshift, we use the parameter  $B_{\text{gc, red}}$  for the measurement of richness.

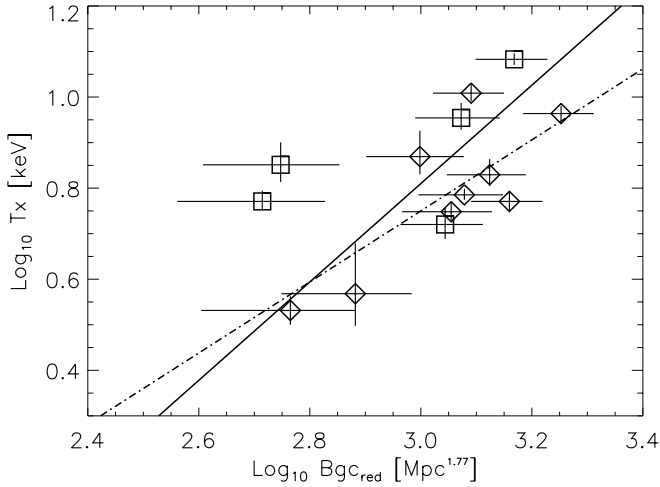


FIG. 9.—log-log plot of  $T_X$  vs.  $B_{gc,red}$  for the clusters in our sample. Error bars represent 68% confidence intervals. The solid line indicates the best-fitting relationship between these two parameters (§ 9), while the dot-dashed line illustrates the previous results of Yee & Ellingson (2003). Squares denote clusters which exhibit significant cool cores.

At the relatively low redshifts of the CNOC clusters, the difference between  $B_{gc}$  and  $B_{gc,red}$  is small. We estimate  $B_{gc,red}$  values by applying small corrections to the original  $B_{gc}$  values of the CNOC clusters (Yee & Ellingson 2003), based on their blue fractions (Ellingson et al. 2001). Most of the corrections are of the order of  $\sim 10\%$ . Values of  $B_{gc,red}$  (in units of  $h_{50}^{-1} \text{ Mpc}^{1.77}$ ), as well as the cluster X-ray luminosities obtained in § 4.1, are given in Table 10. To keep the same scale as previous work using the  $B_{gc}$  parameter, they are computed using  $H_0 = 50 \text{ km s}^{-1} \text{ Mpc}^{-1}$ .

The  $B_{gc}$  values have previously been shown to correlate strongly with the X-ray properties of clusters in this sample (Yee & Ellingson 2003). Here, we reexamine these correlations using improved X-ray data from *Chandra*. Extending the simple relationships expressed in Yee & Ellingson (2003) to  $B_{gc,red}$ , we have

$$B_{gc,red} \propto T_X^{\gamma/2}, \quad (15)$$

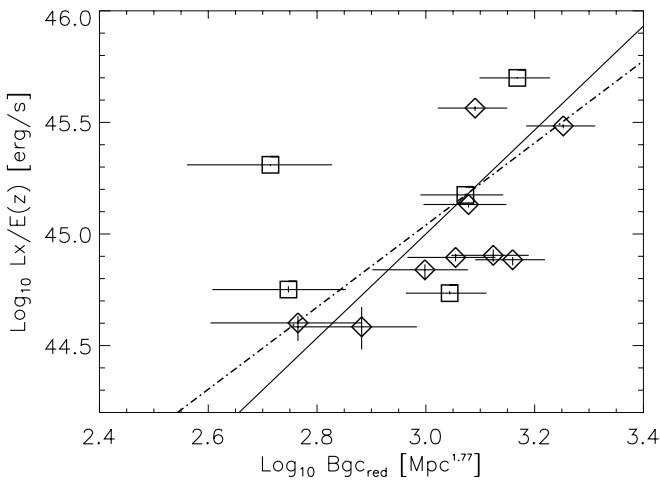


FIG. 10.—log-log plot of  $L_X$  vs.  $B_{gc,red}$  for the clusters in our sample. Error bars represent 68% confidence intervals. The solid line indicates the best-fitting relationship (§ 9), and the dot-dashed line denotes the Yee & Ellingson (2003) result. Squares again denote clusters that exhibit significant cool cores.

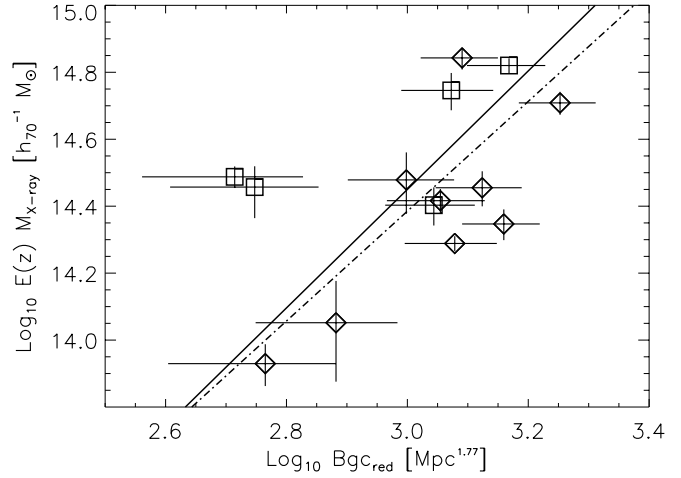


FIG. 11.—log-log plot of X-ray mass estimates vs.  $B_{gc,red}$  for the clusters in our sample. Error bars represent 68% confidence intervals. The solid line represents the best-fitting relationship between these two parameters (§ 9). The dot-dashed line was produced from the Yee & Ellingson (2003) results, scaling their intercept by the average of  $M_{2500}/M_{200}$  for this sample. Squares denote cooling core clusters.

and using our best-fit  $L_X$ - $T_X$  and  $M$ - $T_X$  relationships (§ 8), in combination with equation (15),

$$B_{gc,red} \propto \left[ \frac{L_X}{E(z)} \right]^{\gamma/4.8}, \quad (16)$$

and

$$B_{gc,red} \propto [E(z)M_{2500}]^{\gamma/3.4}. \quad (17)$$

In this section we derive the best-fitting relationships between cluster X-ray properties and  $B_{gc,red}$  for our sample. A generic form for these relationships of

$$\log X = C_1 + C_2 \log B_{gc,red} \quad (18)$$

is adopted, where  $X$  represents the particular property being fit. For  $T_X$ ,  $E(z)M_{2500}$ , and  $L_X/E(z)$ , units of keV, solar masses, and  $10^{44} \text{ ergs s}^{-1}$  were used, respectively. As in Yee & Ellingson (2003) the BCES estimator of Akritas & Bershadsky (1996) was employed.

The results of these fits are all consistent within errors with those of Yee & Ellingson (2003) and are also consistent with the expected value of  $\gamma$  ( $=1.77$ ). The data, with the results of these fits as well as those of Yee & Ellingson (2003) overlaid, are shown in Figures 9–11. Best-fitting parameters of all fits are given in Table 11.

TABLE 11  
FITTING PARAMETERS ( $\Delta = 2500$ )

Relationship	$C_1$	$C_2$
$T_X$ - $B_{gc,red}$ .....	$-2.4 \pm 0.8$	$1.1 \pm 0.3$
$E(z)^{-1}L_X$ - $B_{gc,red}$ .....	$-6 \pm 2$	$2.3 \pm 0.7$
$E(z)M_{2500}$ - $B_{gc,red}$ .....	$9 \pm 2$	$1.8 \pm 0.5$

## 10. SUMMARY AND DISCUSSION

We have presented a comprehensive analysis of *Chandra* observations of 14 medium-redshift ( $0.1709 < z < 0.5466$ ) clusters of galaxies from the CNOC subsample of the EMSS (Table 1). Imaging analysis has provided information on the relative quiescence of each cluster (Fig. 1). The spatial resolution of *Chandra* has allowed us to determine the surface brightness profiles of these clusters down to  $1''$  scales (Fig. 2). This has enabled us to obtain precise models of cluster emission (Table 2), except in the case of MS 0451+02, which displays a considerable amount of substructure. Five clusters in our sample (Abell 2390, MS 0440+02, MS 0839+29, MS 1358+62, and MS 1455+22) exhibit excess emission in their cores, indicating the presence of cool gas. The surface brightnesses of these five clusters are better fit with the inclusion of a second  $\beta$ -component to model the excess core emission (Table 3).

*Chandra*'s  $0''.5$  spatial resolution has enabled us to study the radial distribution of temperatures on small scales ( $\sim 7$ – $100$  kpc) in the inner 150–600 kpc of 11 of these objects (Fig. 3). While nine clusters in our sample have temperature profiles that are consistent with isothermality, the five cooling core clusters (listed above) show clear temperature gradients in their innermost  $\sim 60$ – $200$  kpc. The temperature profiles of these five clusters are consistent with the “universal” temperature profile of Allen et al. (2001).

The energy resolution of the instrument has provided well constrained spectral analyses of the central  $R_{2500}$  ( $\sim 350$ – $760$ ) kpc of each object. Temperatures obtained initially from 300 kpc radius extraction regions began an iterative spectral extraction and fitting process culminating in the determination of robust integrated temperatures, luminosities, and abundances within  $R_{2500}$  (Tables 4 and 5). Cooling core corrected spectra were used to determine global temperatures for the clusters in our sample that exhibit significant cooling. These temperatures were then employed in the spectral determination of integrated luminosities for these objects. Overall, our sample displays temperatures in the range of 3.4–12.1 keV, abundances that range from 0.1–0.8 times the solar value, and unabsorbed bolometric luminosities within  $R_{2500}$  that span  $(4.9$ – $56.1) \times 10^{44}$  ergs  $s^{-1}$ .

Cluster gas and total masses within  $R_{2500}$  and  $R_{200}$  were estimated using the outcomes of spectral and surface brightness fitting, resulting in virialized cluster masses of  $(2.7$ – $21) \times 10^{14} h_{70}^{-1} M_{\odot}$  (Table 7) and respective cluster gas masses of  $(0.13$ – $2.9) \times 10^{14} h_{70}^{-1} M_{\odot}$ . A weighted average of gas mass fractions gives  $f_{\text{gas}} = 0.092 \pm 0.004 h_{70}^{-3/2}$ , resulting in  $\Omega_m = 0.42 \pm 0.02$  (68% confidence, formal error).

Dynamical masses within  $R_{200}$  were calculated via the Jeans equation using velocity dispersions taken from Borgani et al. (1999) (Table 8). Comparisons between X-ray masses and dynamical masses result in a weighted average of  $M_{\text{dyn}}/M_X = 0.97 \pm 0.05$ , indicating good agreement between these two methods; however, a fair amount of scatter is evident ( $\sim 30\%$ ; Fig. 5). Dynamical masses are noticeably larger in the case of clusters that exhibit significant substructure (MS 1006+12 and MS 1008–12), a factor that may be responsible for an overestimation of velocity dispersions (Bird et al. 1995).

Weak-lensing masses within 500  $h_{100}^{-1}$  kpc were obtained for seven of the clusters in our sample. X-ray masses were calculated within this region and compared to the lensing results (Table 9). Although the distribution appears somewhat asymmetric (Fig. 6), a weighted average gives  $M_{\text{lens}}/M_X = 0.99 \pm 0.07$ , with a scatter of  $\sim 30\%$ .

X-ray scaling laws for this sample were investigated in a manner similar to Allen et al. (2001) and Ettori et al. (2004) taking cosmological factors into account. The best-fitting  $L_X$ – $T_X$  relationship for our sample results in an intercept of  $0.13^{+0.08}_{-0.05}$  and a slope of  $2.4 \pm 0.2$  (Fig. 7). While this slope is lower than some estimates (Arnaud & Evrard 1999; Ettori et al. 2004), it is consistent with both Allen et al. (2001) and Ettori et al. (2002). Moderate negative evolution is indicated by this index being greater than that predicted by self-similar models (Voit 2005). The  $M$ – $T_X$  relationship for these clusters also exhibits a somewhat steeper slope than expected, at  $1.7 \pm 0.1$ , with an intercept of  $1.3^{+0.3}_{-0.2} \times 10^{15}$  (Fig. 8).

The best-fitting scaling laws for our sample (listed above) were combined with equation (15), with the ultimate goal of calibrating relationships between red-sequence optical richness ( $B_{\text{gc,red}}$ ) and global cluster parameters ( $T_X$ ,  $L_X$  and  $M_{2500}$ ). We find that  $T_X$  scales relatively well to  $B_{\text{gc,red}}$  with a 40% scatter (Fig. 9). The  $M_{2500}$  values show a scatter of  $\sim 70\%$  (Fig. 11), which is consistent with the  $T_X$ – $B_{\text{gc,red}}$  scatter given that  $M \propto T^{3/2}$ . The  $L_X$ – $B_{\text{gc,red}}$  relationship exhibits a significantly larger scatter at  $\sim 200\%$  (Fig. 10).

Our results indicate that  $B_{\text{gc,red}}$  does exhibit initial promise as a mass indicator. Accurate calibration of a relationship between optical richness and cluster mass will require the use of additional clusters that possess both well-constrained X-ray temperatures and optical richness measurements.

Overall, we find that multiple cluster-mass estimators (dynamics, weak-lensing, and X-ray observations, along with optical richness in the cluster red sequence) are converging for this sample of well-studied clusters. While individual correlations still have significant scatter, there is little evidence for large systematic bias in any of these methods. Cluster characteristics that might be considered problematic for one or more techniques (cluster substructure, merging, and/or the presence of a cool core) appear to perturb these relationships relatively little, as long as high-quality data are obtained and the analysis is tuned to correct for these. In particular, the correlation between cluster temperature and optical richness, the most easily obtained of the mass estimators, is promising. A remaining concern is that X-ray-selected clusters may not prove to be typical of all massive clusters at these redshifts. Additional checks involving clusters covering a broader range of redshift and selection technique (e.g., SZ, optical, weak-lensing) will be necessary to solidify our understanding of the most reliable and efficient methods of cluster mass estimation.

Support for this work was provided by the National Aeronautics and Space Administration through a Graduate Student Research Program (GSRP) fellowship, NGT 5-140, and *Chandra* Awards GO 0-1079X and GO 0-1063B, issued by the *Chandra* X-ray Observatory Center, which is operated by the Smithsonian Astrophysical Observatory for and on behalf of the National Aeronautics Space Administration under contract NAS 8-03060. We would also like to thank Phil Armitage, Mark Bautz, Webster Cash, John Houck, and Richard Mushotzky for their contributions and input.

Some of the data presented in this paper were obtained from the Multimission Archive at the Space Telescope Science Institute (MAST). STScI is operated by the Association of Universities for Research in Astronomy, Inc., under NASA contract NAS 5-26555. Support for MAST for non-*HST* data is provided by the NASA Office of Space Science via grant NAG 5-7584 and by other grants and contracts.

## REFERENCES

- Abell, G. O. 1958, *ApJS*, 3, 211
- Akritas, M. G., & Bershady, M. A. 1996, *ApJ*, 470, 706
- Allen, S. W. 2000, *MNRAS*, 315, 269
- Allen, S. W., & Fabian, A. C. 1997, *MNRAS*, 286, 583
- Allen, S. W., Schmidt, R. W., & Fabian, A. C. 2001, *MNRAS*, 328, L37
- . 2002, *MNRAS*, 334, 11
- Arabadjis, J. S., Bautz, M. W., & Garmire, G. P. 2002, *ApJ*, 572, 66
- Arnaud, K. A. 1996, in *ASP Conf. Ser. 101, Astronomical Data Analysis Software and Systems V*, ed. G. H. Jacoby & J. Barnes (San Francisco: ASP), 17
- Arnaud, M., & Evrard, A. E. 1999, *MNRAS*, 305, 631
- Bahcall, N. A., Fan, X., & Cen, R. 1997, *ApJ*, 485, L53
- Balland, C., & Blanchard, A. 1997, *ApJ*, 487, 33
- Bird, C. M., Mushotzky, R. F., & Metzler, C. A. 1995, *ApJ*, 453, 40
- Böhringer, H., Tanaka, Y., Mushotzky, R. F., Ikebe, Y., & Hattori, M. 1998, *A&A*, 334, 789
- Borgani, S., Girardi, M., Carlberg, R. G., Yee, H. K. C., & Ellingson, E. 1999, *ApJ*, 527, 561
- Carlberg, R. G., Yee, H. K. C., Ellingson, E., Abraham, R., Gravel, P., Morris, S., & Pritchett, C. J. 1996, *ApJ*, 462, 32
- Cen, R. 1997, *ApJ*, 485, 39
- Davis, M., & Peebles, P. J. E. 1983, *ApJ*, 267, 465
- Dickey, J. M., & Lockman, F. J. 1990, *ARA&A*, 28, 215
- Donahue, M., Gaskin, J. A., Patel, S. K., Joy, M., Clowe, D., & Hughes, J. P. 2003, *ApJ*, 598, 190
- Donahue, M., Stocke, J. T., & Gioia, I. M. 1992, *ApJ*, 385, 49
- Eke, V. R., Cole, S., Frenk, C. S., & Henry, J. P. 1998, *MNRAS*, 298, 1145
- Ellingson, E., Lin, H., Yee, H. K. C., & Carlberg, R. G. 2001, *ApJ*, 547, 609
- Ettori, S. 2000, *MNRAS*, 311, 313
- Ettori, S., De Grandi, S., & Molendi, S. 2002, *A&A*, 391, 841
- Ettori, S., & Lombardi, M. 2003, *A&A*, 398, L5
- Ettori, S., Tozzi, P., Borgani, S., & Rosati, P. 2004, *A&A*, 417, 13
- Fukugita, M., Hogan, C. J., & Peebles, P. J. E. 1998, *ApJ*, 503, 518
- Gioia, I. M., Henry, J. P., Maccacaro, T., Morris, S. L., Stocke, J. T., & Wolter, A. 1990, *ApJ*, 356, L35
- Gladders, M. D., & Yee, H. K. C. 2005, *ApJS*, 157, 1
- Henry, J. P. 2004, *ApJ*, 609, 603
- Henry, J. P., Gioia, I. M., Maccacaro, T., Morris, S. L., Stocke, J. T., & Wolter, A. 1992, *ApJ*, 386, 408
- Hoekstra, H. 2001, *A&A*, 370, 743
- Levine, E. S., Schulz, A. E., & White, M. 2002, *ApJ*, 577, 569
- Lewis, A. D., Ellingson, E., Morris, S. L., & Carlberg, R. G. 1999, *ApJ*, 517, 587
- Longair, M. S., & Seldner, M. 1979, *MNRAS*, 189, 433
- Matsumoto, H., Tsuru, T. G., Fukazawa, Y., Hattoir, M., & Davis, D. S. 2000, *PASJ*, 52, 153
- Metzler, C. A., White, M., & Loken, C. 2001, *ApJ*, 547, 560
- Mohr, J. J., Reese, E. D., Ellingson, E., Lewis, A. D., & Evrard, A. E. 2000, *ApJ*, 544, 109
- Mushotzky, R. F., & Loewenstein 1997, *ApJ*, 481, L63
- Neumann, D. M., & Böhringer, H. 1997, *MNRAS*, 289, 123
- Spergel, D. N., et al. 2006, *ApJ*, submitted (astro-ph/0603449)
- Van der Marel, R. P., Magorrian, J., Carlberg, R. G., Yee, H. K. C., & Ellingson, E. 2000, *AJ*, 119, 2038
- van Dokkum, P. G., Franx, M., Kelson, D. D., & Illingworth, G. D. 1998, *ApJ*, 504, L17
- Voit, G. M. 2005, *Rev. Mod. Phys.*, 77, 207
- White, S. D. M., Navarro, J. F., Evrard, A. E., & Frenk, C. S. 1993, *Nature*, 366, 429
- Yee, H. K. C., & Ellingson, E. 2003, *ApJ*, 585, 215
- Yee, H. K. C., Ellingson, E., Abraham, R. G., Gravel, P., Carlberg, R. G., Smecker-Hane, T. A., Schade, D., & Rigler, M. 1996a, *ApJS*, 102, 289
- Yee, H. K. C., Ellingson, E., & Carlberg, R. G. 1996b, *ApJS*, 102, 269
- Yee, H. K. C., & Lopez-Cruz, O. 1999, *AJ*, 117, 1985